Using the Kriging Response Surface Method for the Estimation of Failure Values of Carbon-Fibre-Epoxy Subsea Composite Flowlines under the Influence of Stochastic Processes

Yihan Xing [1,*], **Wenxin Xu** [1] **and Valentina Buratti** [2]

1 Department of Mechanical and Structural Engineering and Materials Science, Faculty of Science and Technology, University of Stavanger, 4021 Stavanger, Norway; xuwenxin956401@outlook.com
2 Aibel AS, 4313 Sandnes, Norway; valentina.buratti@aibel.com
* Correspondence: yihan.xing@uis.no

Abstract: This paper investigates the use of the Kriging response surface method to estimate failure values in carbon-fibre-epoxy composite flow-lines under the influence of stochastic processes. A case study of a 125 mm flow-line was investigated. The maximum stress, Tsai-Wu and Hashin failure criteria was used to assess the burst design under combined loading with axial forces, torsion and bending moments. An extensive set of measured values was generated using Monte Carlo simulation and used as the base case population to which the results from the response surfaces was compared. The response surfaces were evaluated in detail in their ability to reproduce the statistical moments, probability and cumulative distributions and failure values at low probabilities of failure. In addition, the optimisation of the response surface calculation was investigated in terms of reducing the number of input parameters and size of the response surface. Finally, a decision chart that can be used to build a response surface to calculate failures in a carbon fibre-epoxy-composite (CFEC) flow-line was proposed based on the findings obtained. The results show that the response surface method is suitable and can calculate failure values close to that calculated using a large set of measured values. The results from this paper provide an analytical framework for identifying the principal design parameters, response surface generation, and failure prediction for CFEC flow-lines.

Keywords: composite material; kriging; response surface; optimisation; failure analysis

1. Introduction

Subsea flow-lines play a vital role in the subsea system. They transport production/injection fluids from subsea wells to subsea manifolds, and vice versa. A higher number of deep-water oil and gas reservoirs are exploited in recent developments experienced in the oil and gas industry. This increased the average depth of oil wells drilled from 1108 m in 1949, and to 1818 m in 2008 [1]. At the same time, the oil and gas trunk pipeline's total length was expected to increase from 1.9 million km to 2.2 million km between 2019 and 2023 [2]. This increase in distance and water depth would lead to higher associated capital and operating costs. The average pipeline cost increased from $94,000 per inch-mile in 2011 to $155,000 per inch-mile in 2002, according to ICF International [3]. One cost-effective solution gaining popularity in the subsea industry is to utilise composite materials instead of the traditionally used steel material for the subsea flow-line. Several projects that have utilised composite flow-lines are Alder, Åsgard, and West Lutong fields. Composite material has long been utilised in the aerospace and automotive industries for various applications. Some applications include using it for components such as the aircraft tail, wings and propellers, boat and scull hulls, storage tanks. They are sought after for the high strength-to-weight ratio and the customizable material directional strength properties, which can be adjusted by designing the laminate layout according to the intended application. Composite materials are not new in the subsea industry. They have been utilised

to make subsea protection covers and ROV buckets. Their corrosion resistance properties, in addition to their strength properties, make them particularly attractive in the offshore and subsea oil and gas industry. These properties make composite materials an attractive choice in high-performance subsea flow-line applications where long reaches, deep waters, high loads and high temperatures are encountered.

Carbon-fibre epoxy composite (CFEC), which consists of an epoxy matrix with carbon fibres, is a commonly used composite material when a high strength to weight ratio is desired. The epoxy matrix protects the fibres from the external environment and transfers the load between the fibres, while the fibres provide strength and stiffness to the component. As presented in Table 1, CFEC is nearly five times lighter and two times stronger than steel. This allows CFEC structures to carry larger loads than metal structures of the same weight. Moreover, as with all composite materials, the excellent corrosion properties make CFEC suitable for use in harsh environments such as subsea oil and gas applications. The epoxy carbon UD in Table 1 has a fibre volume fraction (FVF) of 60%.

Table 1. Comparison of epoxy carbon UD (230GPa) and steel AISI 4130.

	Yield Strength (GPa)	Ultimate Tensile Strength (GPa)	Density (g/cm^3)	Strength to Weight Ratio
Epoxy carbon UD	-	2.231	1.49	1.497
Steel, AISI 4130	0.95	1.11	7.85	0.141

The anisotropic nature of CFEC materials demands very comprehensive and robust stress analyses. Various authors have published several pipeline stress analysis studies. Some examples include Yang [4], who analysed the stresses at composite pipe joints under tensile loading, and Jha et al. [5], who investigated the stresses in composite flexibles for deep-water applications. Due to the complex subsea terrain, current and other factors, the subsea CEFC flow-line experiences complex combined loading. In addition, the joint action of random parameters from loads, materials, and geometry means that it may be necessary to apply stochastic models in engineering design. Some authors have previously presented stochastic processes used in pipeline engineering problems. These include Bazan et al. [6], who studied stochastic processes to predict corrosion growth in pipelines, and Oliveira et al. [7], who used the probabilistic analysis method to investigate the collapse pressure of corroded pipelines. However, applying stochastic considerations in engineering design problems is typically not widely adopted. This is mainly because it requires a large sample size, i.e., a large set of realisation values. This involves time resources which can be valuable in engineering projects.

The response surface methodology is an approach that calculates an approximate result based on a response surface. The response surface is modelled by sample results calculated from simulations or measured in real life. This method requires fewer samples than the traditional approach when applied in stochastic structural analysis. Some examples of response surface methods used in engineering problems are presented here. Jia et al. [8] studied the Kriging-base response surface application in structure reliability. Simpson et al. [9] performed a comparison of the response surface and Kriging models when utilised in multidisciplinary design optimisation. Gupta et al. [10] suggested a response surface method that was improved using failure probability determination. These studies showed that the response surface is a convenient engineering analysis and optimisation tool. However, the utilisation of the response surface does require careful consideration since the response results are approximate. Many factors affect accuracy. These include the response surface type, chosen parameters, refinement method, etc.

To the authors' knowledge, there have been no prior studies using response surfaces as a tool to calculate failure values for CEFC flow-lines in a more efficient manner. This paper studies the influence of stochastic processes on the Kriging response surface method to predict failure rates in a CFEC flow-line subjected to combined loading. The Tsai-Wu [11], maximum stress and Hashin [12] failure criteria were used to quantify failure of the composite material. An extensive set of measured values was generated using Monte Carlo

simulation and used as the base case population to which the results from the response surfaces were compared. The response surfaces were evaluated in detail in their ability to reproduce the statistical moments, probability and cumulative distributions and failure values at low probabilities of failure. In addition, the optimisation of the response surface calculation was investigated in terms of reducing the number of input parameters and size of the response surface. Finally, a decision chart that can be used to build a response surface to calculate failures in a CFEC flow-line was proposed based on the findings obtained. The modelling and the design optimisation were performed using ANSYS Composite Pre/Post, Mechanical and DesignXplorer [13].

2. Preliminaries

2.1. Failure Criteria

Failure criteria are used in engineering to evaluate structural integrity. Generally, failure criteria compare the stresses experienced by structure to their allowable stress values. When the ratio between the two stresses is larger than 1, the component is usually considered to fail. Composite materials' failure criteria can be grouped into two categories: (i) non-interactive failure criteria and (ii) interactive failure criteria. Non-interactive failure criteria, as the name suggests, assumes no interaction between stress or strain tensor components, i.e., the tensor components are evaluated individually.

One example is the maximum stress criterion. In contrast, Tsai-Wu [11] and Hashin [12] are two examples of interactive failure criteria. Interactive failure criteria describe the failure value as a combined function of the stress or strain tensor components. The three failure criteria mentioned above were chosen to study the burst design of the CFEC flow-line in this paper. It is noted that since the classical laminate theory is used, the stresses component in the z-direction was neglected, i.e., $\sigma_3 = \tau_{23} = \tau_{13} = 0$ in the following sections.

2.1.1. Maximum Stress Failure Criterion

The maximum stress failure criterion is a conservative and commonly used criterion for composite materials [14]. The failure occurs when the stresses in any principle direction exceed the material strength in that direction. The failure value is calculated using Equation (1).

$$f = max\left(\left|\frac{\sigma_1}{X}\right|, \left|\frac{\sigma_2}{Y}\right|, \left|\frac{\sigma_3}{Z}\right|, \left|\frac{\tau_{12}}{S}\right|, \left|\frac{\tau_{13}}{R}\right|, \left|\frac{\tau_{23}}{Q}\right|\right) \tag{1}$$

where:

$$X = \begin{cases} \sigma_{uc1}, \sigma_1 < 0 \\ \sigma_{ut1}, \sigma_1 \geq 0 \end{cases}, \quad S = \tau_{u12}$$

$$Y = \begin{cases} \sigma_{uc2}, \sigma_2 < 0 \\ \sigma_{ut2}, \sigma_2 \geq 0 \end{cases}, \quad R = \tau_{u13} \tag{2}$$

$$Z = \begin{cases} \sigma_{uc3}, \sigma_3 < 0 \\ \sigma_{ut3}, \sigma_3 \geq 0 \end{cases}, \quad Q = \tau_{u23}$$

2.1.2. Tsai-Wu Failure Criterion

The Tsai-Wu failure criterion [11] is based on the work of Gol'denblat and Koponov [15]. The criterion assumes the existence of a failure surface and distinguishes between the compressive and tensile strength in the ply failure prediction. The failure criterion uses the following quadratic formulation presented in Equation (3).

$$f = \frac{\sigma_1^2}{\sigma_{ut1}\sigma_{uc1}} + \frac{\sigma_2^2}{\sigma_{ut2}\sigma_{uc2}} + \frac{\tau_{12}^2}{\tau_{u12}^2} + \sigma_1\left(\frac{1}{\sigma_{ut1}} - \frac{1}{\sigma_{uc1}}\right) + \sigma_2\left(\frac{1}{\sigma_{ut2}} - \frac{1}{\sigma_{uc2}}\right) + 2F_{12}\sigma_1\sigma_2 \tag{3}$$

F_{12} is a user-specified parameter and is only associated with principle stresses σ_1 and σ_2. One commonly used form of F_{12} is presented in Equation (4).

$$F_{12} = -\frac{1}{2}\sqrt{\left(\frac{1}{\sigma_{ut1}} - \frac{1}{\sigma_{uc1}}\right)\left(\frac{1}{\sigma_{ut2}} - \frac{1}{\sigma_{uc2}}\right)} \tag{4}$$

F_{12} is also commonly obtained using bi-axial tests. Some examples can be found in Clouston et al. [16] and Li et al. [17].

2.1.3. Hashin Failure Criterion

The Hashin failure criterion [12] was initially developed for unidirectional polymeric composites. The failure criterion distinguishes between three different failure modes: fibre failure, matrix failure, and interlaminate failure, respectively. These failure modes are illustrated in Figure 1.
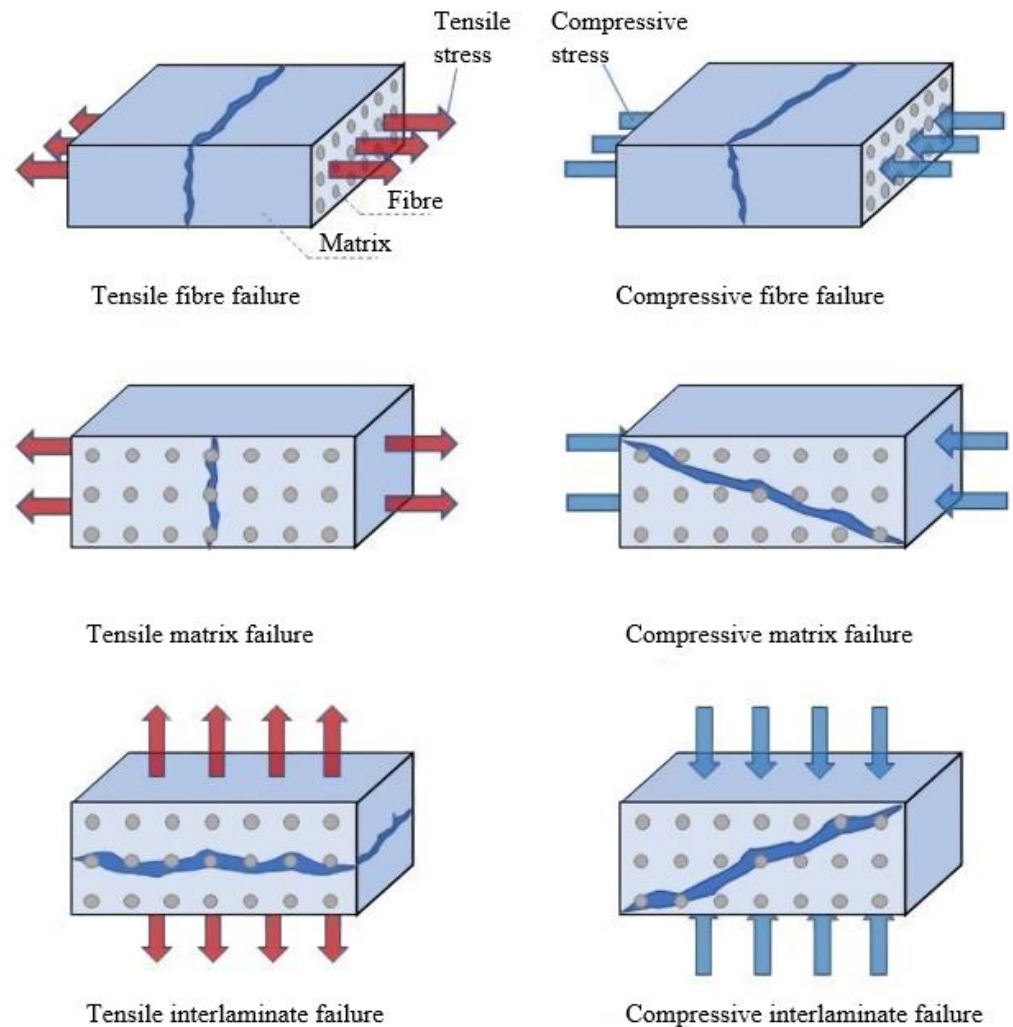
Figure 1. Illustration of the various failure modes in the Hashin failure criterion.

The criterion for tensile fibre failure is presented in Equation (5).

$$f = \left(\frac{\sigma_1}{\sigma_{ut1}}\right)^2 + \left(\frac{\tau_{12}}{\tau_{u12}}\right)^2, \sigma_1 \geq 0 \tag{5}$$

The criterion for compressive fibre failure is presented in Equation (6).

$$f = -\frac{\sigma_1}{\sigma_{ut1}}, \ \sigma_1 < 0 \tag{6}$$

The criterion for tensile matrix failure is presented in Equation (7).

$$f = \left(\frac{\sigma_2}{\sigma_{ut2}}\right)^2 + \left(\frac{\tau_{23}}{\tau_{u23}}\right)^2 + \left(\frac{\tau_{12}}{\tau_{u12}}\right)^2 + \left(\frac{\tau_{13}}{\tau_{u13}}\right)^2 \tag{7}$$

The criterion for compressive matrix failure is presented in Equation (8).

$$f = \left(\frac{\sigma_2}{2\tau_{u23}}\right)^2 + \left(\frac{\tau_{23}}{\tau_{u23}}\right)^2 + \left(\frac{\tau_{12}}{\tau_{u12}}\right)^2 + \left[\left(\frac{\sigma_{uc2}}{2\tau_{u23}}\right)^2 - 1\right]\frac{\sigma_2}{\sigma_{uc2}} \tag{8}$$

The criterion for tensile interlaminate failure is presented in Equation (9).

$$f = \left(\frac{\sigma_3}{\sigma_{uc3}}\right)^2 + \left(\frac{\tau_{13}}{\tau_{u13}}\right)^2 + \left(\frac{\tau_{23}}{\tau_{u23}}\right)^2, \sigma_3 < 0 \tag{9}$$

The criterion for compressive interlaminate failure is presented in Equation (10).

$$f = \left(\frac{\sigma_3}{\sigma_{ut3}}\right)^2 + \left(\frac{\tau_{13}}{\tau_{u13}}\right)^2 + \left(\frac{\tau_{23}}{\tau_{u23}}\right)^2, \sigma_3 \geq 0 \tag{10}$$

2.1.4. Calculation of Failure Values

The failure values were calculated using ANSYS Composite Pre/Post. The ACP solution then showed the failure results and the failure modes. As presented in Sections 2.1.1–2.1.3, three failure criteria have different failure modes. For the maximum stress, the failure modes are associated with σ_1, σ_2 and σ_3, while the Tsai-Wu failure criteria do not distinguish between the failure modes. Hashin failure criteria are matrix failure, fibre failure and interlaminate failure. The failure values were calculated at the middle of the flow-line.

2.2. Parameter Correlation

In this paper, the Spearman [18] correlation method was applied to identify the most critical parameters to be included in the response surfaces; the response surface methodology is presented in Section 2.3. The Spearman correlation method is a rank-order method that calculates the monotonic relationship between two ranked variables as presented in Equation (11).

$$\rho_{rgX,rgY} = \frac{cov(g_X, rg_Y)}{SD_{rg_X} SD_{rg_Y}} \tag{11}$$

The calculated correlation coefficient varies from −1.0 to 1.0 and measures the statistical coupling between two parameters, *x* and *y*. The values of the computed coefficient can be interpreted as follows:

- 0.0 to 0.2—Slightly correlated, the relationship is almost negligible.
- 0.2 to 0.4—Lowly correlated, but the relationship is definite.
- 0.4 to 0.6—Moderately correlated, the relationship is substantial.
- 0.6 to 0.8—Highly correlated, the relationship is marked
- 0.8 to 1.0—Very highly correlated, the relationship is very dependable

A positive coefficient means that the output parameter increases when the input parameter increases, and vice versa. The correlation matrix is an n × n matrix that consists of n² correlation coefficients describing the correlation among n design parameters. The matrix provides an overview of which parameters influence the output variables more. The

top 20 parameters with the highest coefficient values were included in the set of parameters used to generate the response surface model.

2.3. Response Surface Methodology

Box and Wilson [19] were the first to propose the response surface methodology in 1951. They used mathematical modelling to approximate the relationship between one or more input parameters and one or more output variables. This means (Output1, Output2, . . .) = F (Input1, Input2, . . .) where F is the response surface. The response surface methodology is advantageous to describe model responses when the detailed function describing the input parameters to the output variables is complex and usually unknown. This is because the response surface methodology approximates the function without knowing the details.

This paper's applied response surface method is the Kriging response surface method reference [20]. It is an interpolation method that interpolates the values generated by the Gaussian process, which is governed by prior covariances. It is similar to the inverse distance weighting method, i.e., it weighs the surrounding measured values to calculate a predicted result at an unknown location. The general formula for the Kriging response surface method is presented in Equation (12).

$$\hat{Z}(s_0) = \sum_{i=1}^{n} \lambda_i \hat{Z}(s_i) \qquad (12)$$

where $Z(s_i)$ is the measured value at the ith location, λ_i is an unknown weight for the measured value at the ith location, s_0 is the predicted location, and n is the number of measured values.

The response surface tool in ANSYS uses the most-correlated parameters identified from the correlation matrix to generate a required size of measured values. This process is called the design of experiment. An example of a design of experiment applied to foreign object damage on 7075-T6 can be found in Arcieri et al. [21]. The central composite design method [19] was used in this paper. A larger response surface requires a larger design of experiment exercise, i.e., a more significant number of measured values. Verification points were calculated after the response surface was generated. The values from the verification points are checked against the measured values using predicted relative error values as defined in Equation (13).

$$\text{Predicted relative error} = \frac{\text{Predicted error}}{\text{Maximum known value} - \text{Minimum known value}} \times 100\% \qquad (13)$$

where:

$$\text{Predicted error} = \frac{\text{Predicted value} - \text{Measured value}}{\text{Measured value}} \qquad (14)$$

As observed in Equation (13), the predicted relative error is a value that is normalised by the known maximum variation of the output parameter. This allows for easy comparison across all output parameters in the design space. A predicted relative error of 5% was used in this paper. The response surface is refined iteratively with more measured values from the experiments until the predicted relative error of all output parameters falls below the threshold.

3. Case Study of the Burst Design of a Subsea CFEC Flowline

3.1. General Properties

The flow line studied in this paper had an outer diameter, OD = 125 mm, and a wall thickness, t = 6 mm. There were 30 plies, each with a ply thickness, t_{ply} = 0.2 mm. The fibre orientation was $+/-45°$. The material properties of the ply were taken from the Ansys material library and are presented in Table 2. The stacking sequence is illustrated in Figure 2.

Table 2. Material data—Ply (Prepreg Epoxy Carbon UD 230 GPa).

Material Property	Symbol	Value	Unit
Elastic Modulus	E_1, E_2, E_3	121,000, 8600, 8600	MPa
Shear Modulus	G_{12}, G_{23}, G_{13}	4700, 3100, 4700	MPa
Poisson's Ratio	$\nu_{12}, \nu_{23}, \nu_{13}$	0.27, 0.4, 0.27	-
Tensile Strength	$\sigma_{ut1}, \sigma_{ut2}, \sigma_{ut3}$	2231, 29, 29	MPa
Compressive Strength	$\sigma_{uc1}, \sigma_{uc2}, \sigma_{uc3}$	$-1082, -100, -100$	MPa
Shear Strength	$\tau_{u12}, \tau_{u23}, \tau_{u13}$	60, 32, 60	MPa
Tsai-Wu Constants	F_{12}, F_{23}, F_{13}	$-1, -1, -1$	-
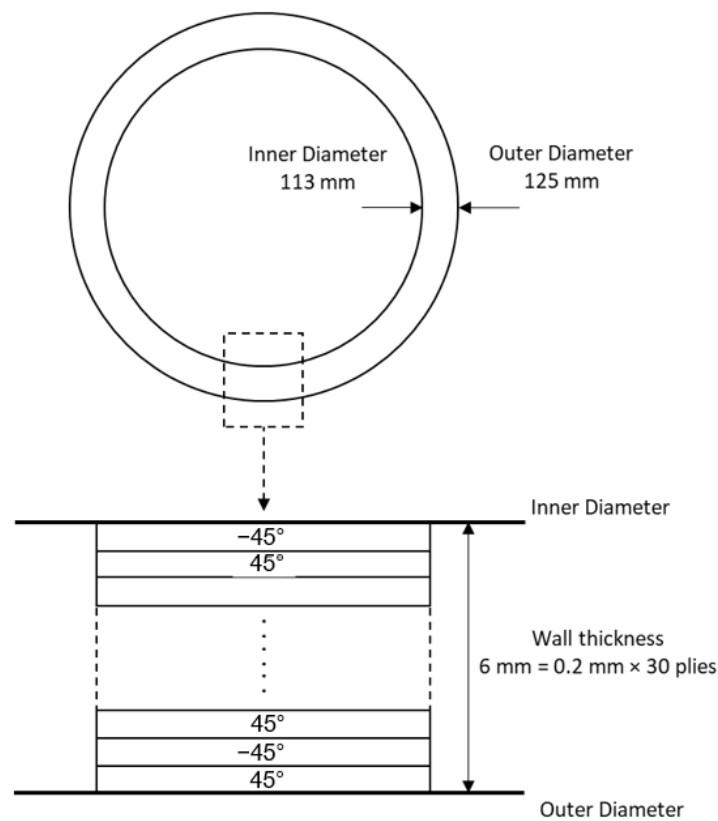
Figure 2. Stacking sequence.

3.2. Nominal Load Values

The nominal load values applied were an internal pressure of 6.9 MPa, an axial force of 20 kN, a torsion moment of 2 kN·m, and a bending moment of 2 kN·m. An internal pressure of 6.9 MPa or 69 bars was indicative of a flow-line under normal operating conditions. The failure criteria values corresponding to the nominal loads are shown in Table 3. The finite element model used is described in Section 3.3.

Table 3. Failure values corresponding to nominal loads.

	Maximum Stress	Tsai-Wu	Hashin
Failure Criterion Value	0.516	0.613	0.563
Failure Mode	σ_2 exceeded	-	Matrix failure

3.3. Finite Element Model

A long section of the flow-line measuring 2000 mm was simulated. This was considered long enough not to have any consequence from the end effects from the applied loads and boundary conditions. The results at the midpoint of the flow-line were assessed, i.e.,

the failure values at this location were used in the study. The finite element simulations were performed using ANSYS R17.0 [13].

3.3.1. Loads and Boundary Conditions

Figure 3 presents the loads and boundary conditions applied. Load A is the internal pressure. Load B is the fixed support applied on the right edge of the flow-line. Load E is the end cap force (Load E) applied on the flow-line's left edge. Load C, Load D, and Load F are axial force, torsion, and bending. They were applied to the left edge.
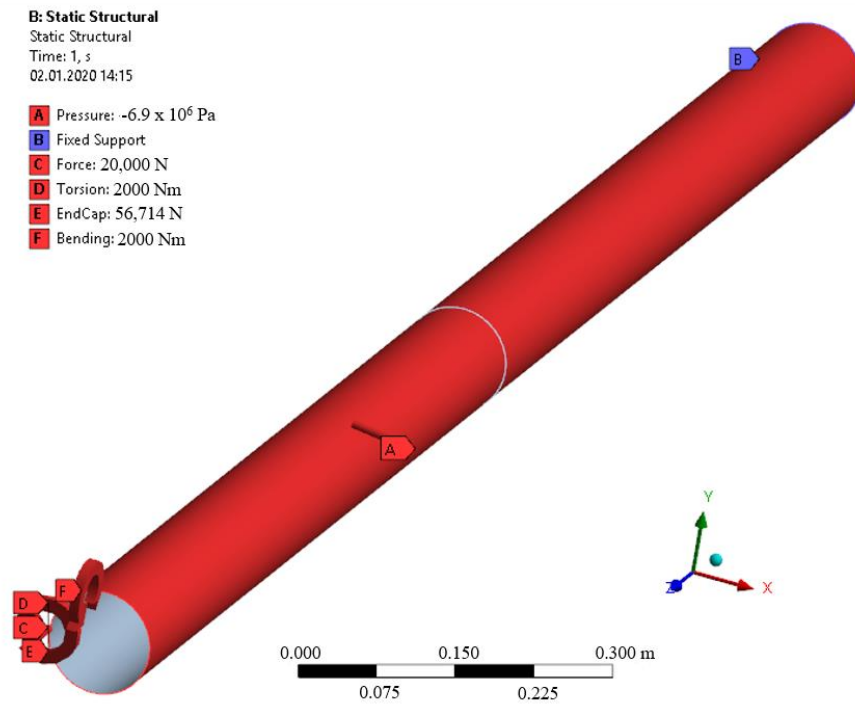
Figure 3. Loads and Boundary Conditions.

3.3.2. Mesh Refinement Study

The results for the mesh refinement study are presented in Table 4 and Figure 4. The nominal load values given in Section 3.2 were used in the mesh refinement study. The 4-node SHELL181 element [13] is used. The element size used in this paper was 10 mm; the mesh details are presented in Figure 5. It is observed from Table 4 that an element size of 30 mm was sufficiently fine to produce converged failure values for all three failure criteria: maximum stress, Tsai-Wu and Hashin.

Table 4. Cases studied for mesh refinement study.

Element Size (mm)	No. of Elements	No. of Nodes
30	900	912
25	1040	1053
20	1536	1552
15	2803	2821
10	6430	6432
5	25,344	25,408
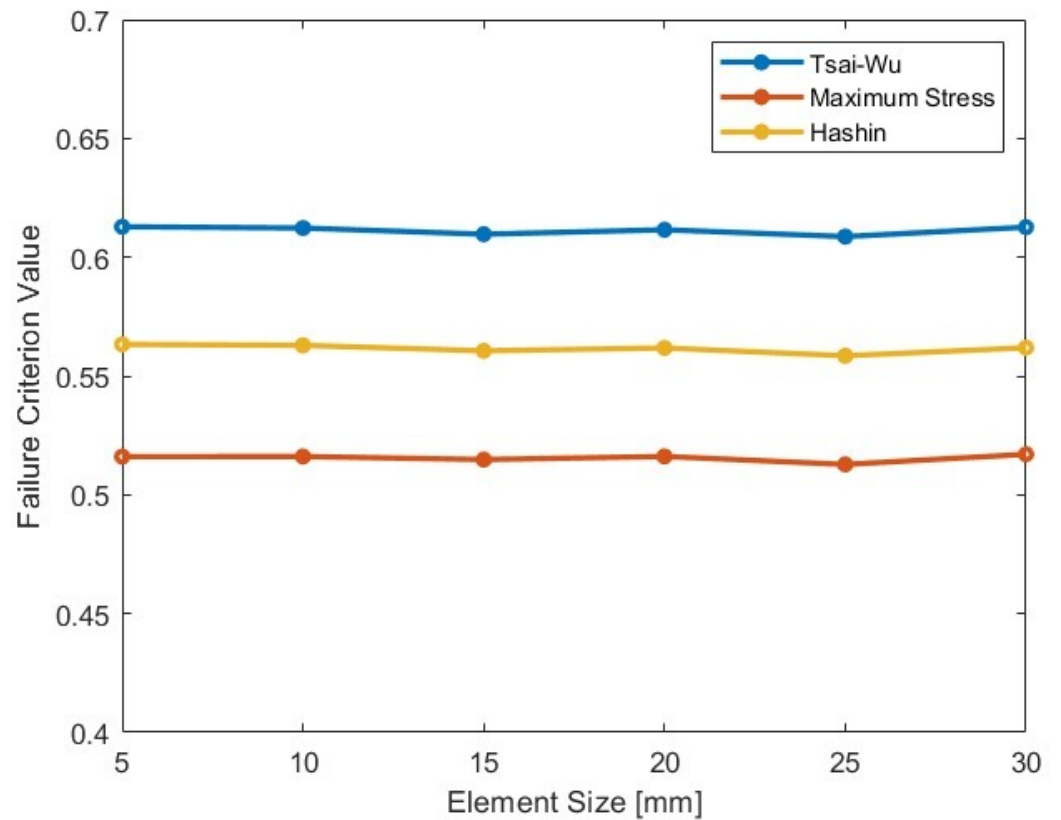
Figure 4. Results of mesh refinement study.
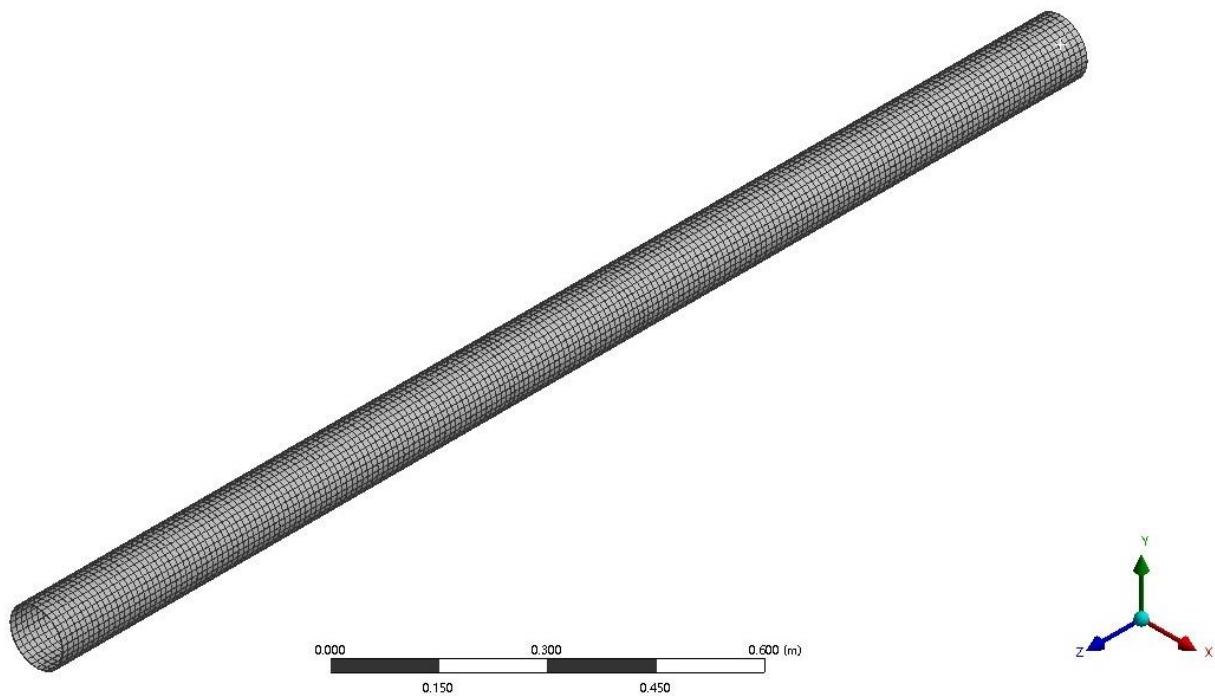
Figure 5. Mesh details, 10 mm element size, 6430 SHELL181 elements with 6432 nodes.

3.4. Generation of Measured Values

The material parameters of Prepreg epoxy carbon UD 230 GPa were taken from the Ansys material library and used as the mean values. The standard deviation was assumed to be 3% of the mean values, i.e., the coefficient of variation was 0.03. This set of parameters

was named the base case in this paper and are presented in Table 5. The input parameters are normally distributed.

Table 5. Mean and standard deviation of input parameters used in base case.

Parameter	Symbol	Unit	Mean	Standard Deviation
Elastic Modulus	E_1	MPa	121,000	3630
	E_2, E_3	MPa	8600	258
Poisson's Ratio	ν_{12}, ν_{13}	-	0.27	0.0081
	ν_{23}	-	0.4	0.012
Shear Modulus	G_{13}	MPa	4700	141
	G_{23}	MPa	3100	93
Tensile Strength	σ_{ut1}	MPa	2231	66.93
	$\sigma_{ut2}, \sigma_{ut3}$	MPa	29	0.87
Compressive Strength	σ_{uc1}	MPa	−1082	−32.46
	$\sigma_{uc2}, \sigma_{uc3}$	MPa	−100	−3
Shear Strength	τ_{u12}, τ_{u13}	MPa	60	1.8
	τ_{u23}	MPa	32	0.96
Internal pressure	P	MPa	−6.9	−0.207
Axial Force	A	N	20,000	600
Bending	B	N·m	2000	60
Torsion	T	N·m	2000	60
Tsai-Wu Constants	F_{12}, F_{23}, F_{13}		0	0.3
Diameter	D	mm	125	8.75
Thickness	t	mm	0.2	0.01

Using the values in Table 5, the base case population of measured values was generated using Monte Carlo simulation. Examples of the cumulative probability distributions are plotted in Figures 6–8 for the elastic modulus E_1, diameter D and internal pressure P, respectively. The population size was 500, chosen based on a convergence study presented in Section 3.4.1. The population size was sufficiently large that converged statistical moments were achieved.
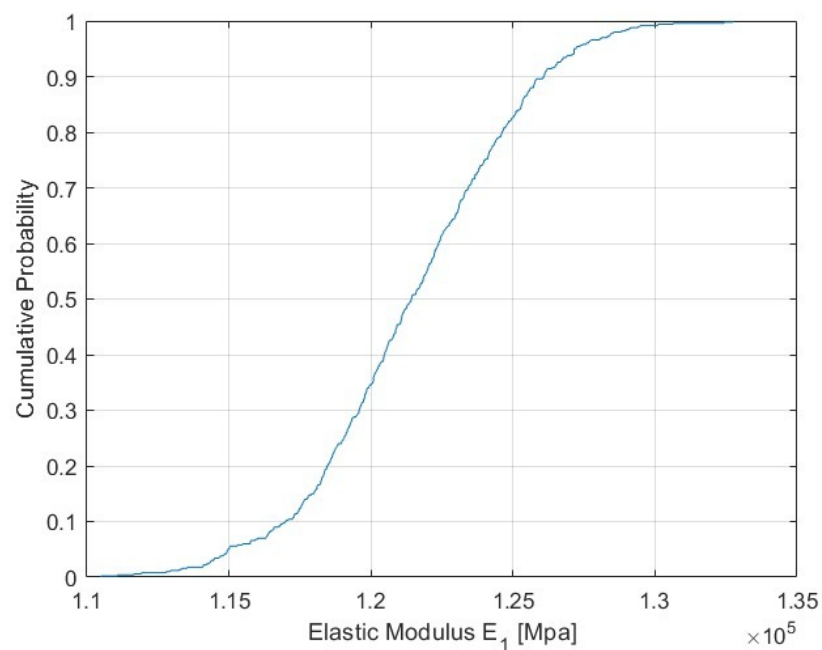
Figure 6. Cumulative probability distribution of elastic modulus E_1.
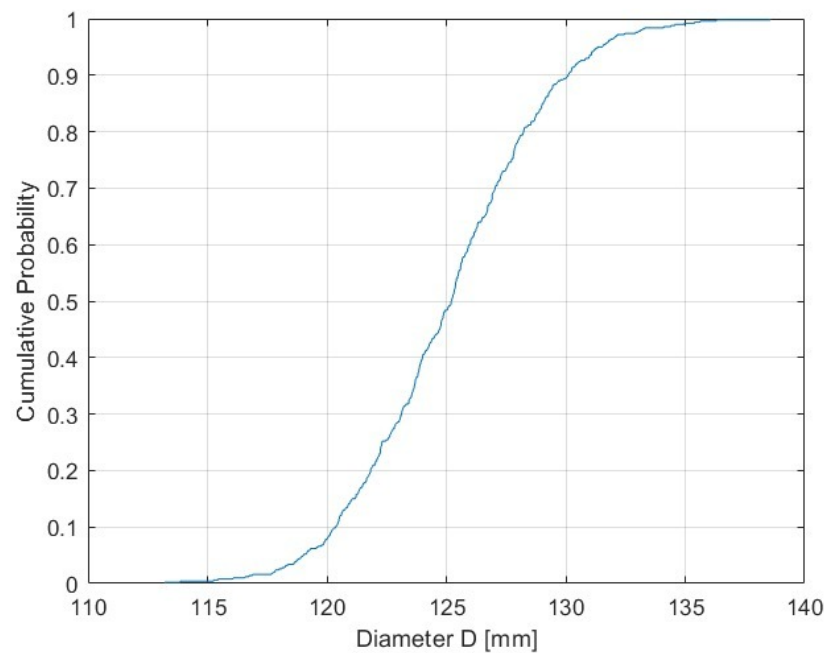
Figure 7. Cumulative probability distribution of diameter *D*.
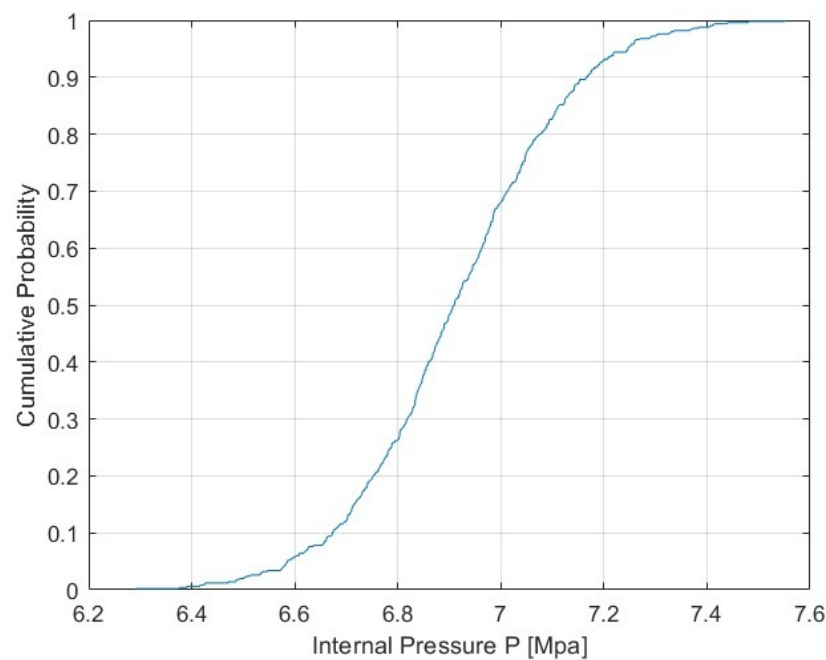
Figure 8. Cumulative probability distribution of internal pressure *P*.

3.4.1. Convergence Study on Population Size

A convergence study was performed to select a large enough population size to obtain converged statistical moments. Figure 9 presents the mean, standard deviation, skewness and kurtosis values versus the sample size. Figure 10 presents the percentage difference for the same statistical moments compared to when the population size is 500. The percentage difference is calculated using the formula given in Equation (15).

$$\% \text{ Difference} = \frac{Current\ value - Value\ @\ N = 500}{Value\ @\ N = 500} \times 100\% \tag{15}$$
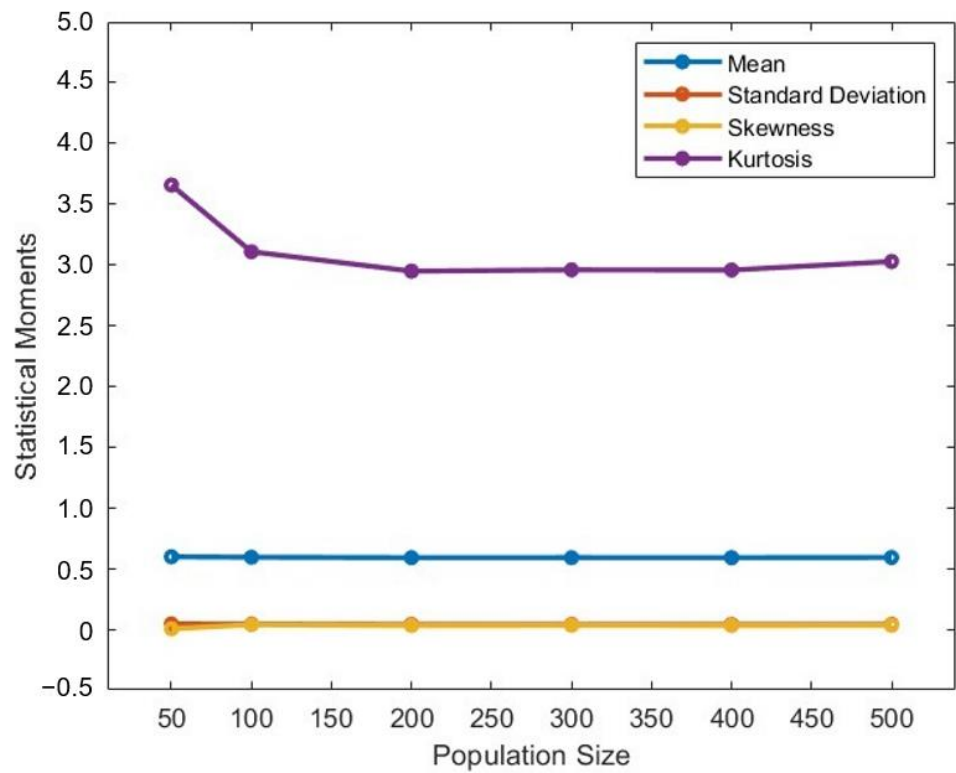
Figure 9. Values of statistical moments vs. population size.
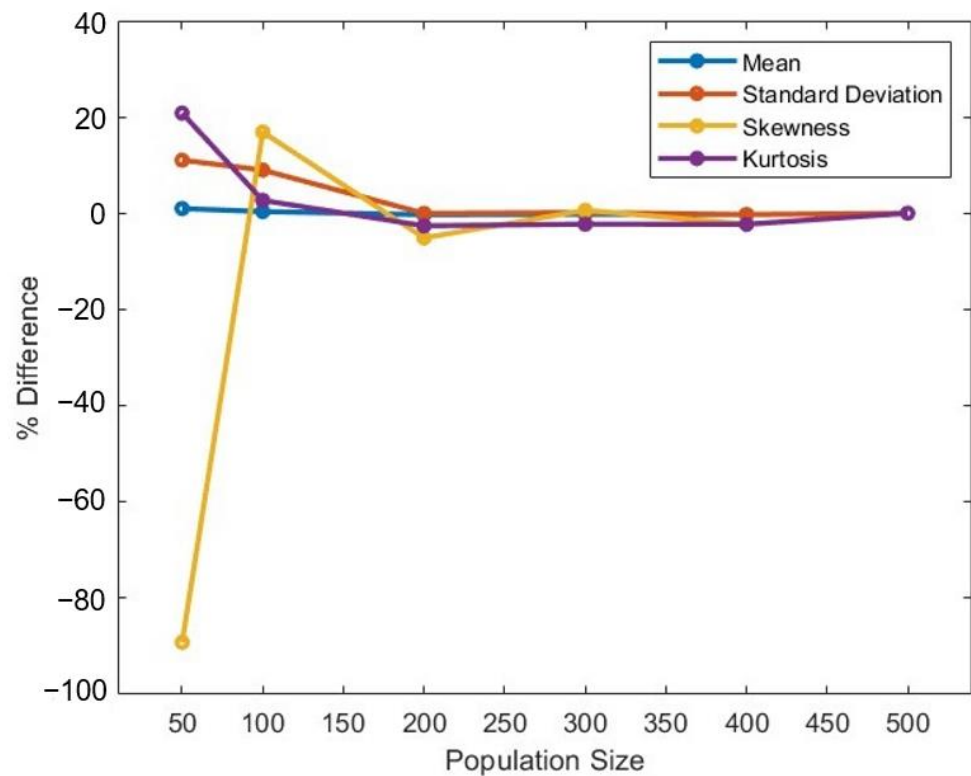
Figure 10. % Difference of values of statistical moments vs. population size compared to N = 500.

The results presented in Figures 9 and 10 show that converged statistical moments are obtained for a population size larger than 200. A population size of 500 is used in this paper.

3.4.2. Fitting Statistical Models to Measured Values

Statistical models fitted to the results were used to calculate the exceedance probabilities, i.e., failure rates. This section presents the various statistical models used in the fitting. The Matlab distribution fitting tool was used. Four types of distributions, namely Exponential, Weibull, Normal and Lognormal, were fitted and compared with the measured values, as shown in Figures 11 and 12. The corresponding R^2 values are presented in Table 6. As previously mentioned, the population size, i.e., the size of the set of measured values, was 500.
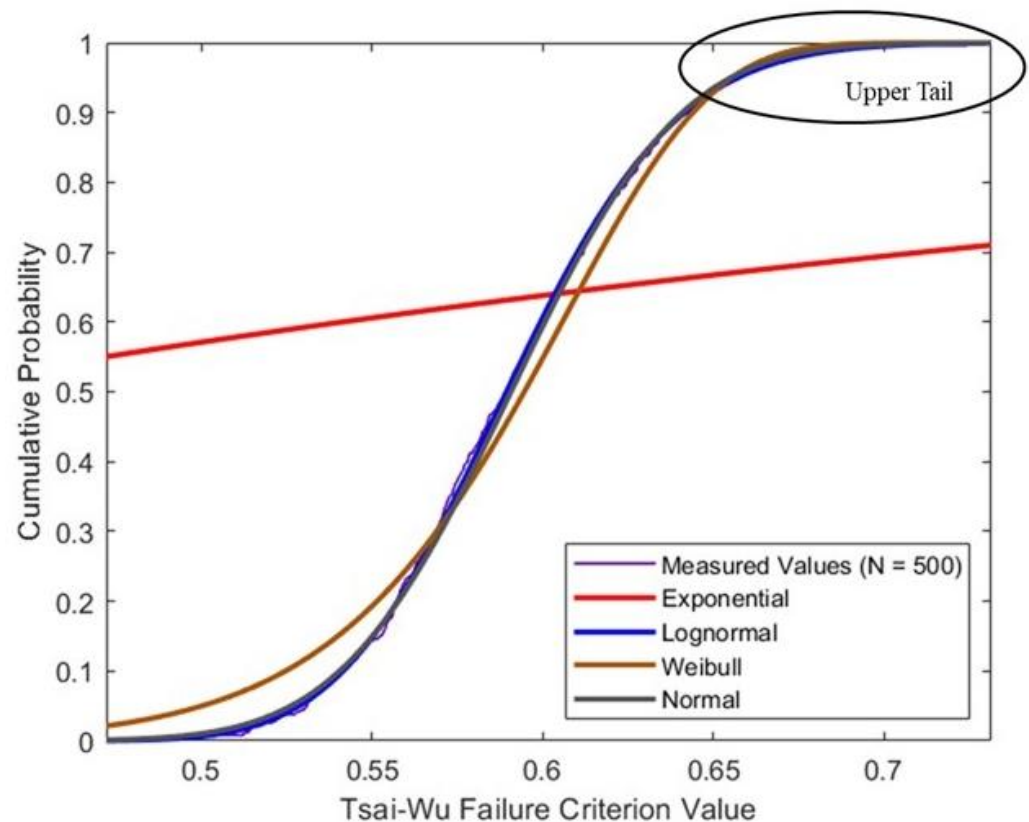
Figure 11. Statistical models fitted to measured values.

The results show that the Lognormal and Normal distributions fit the measured values better. In contrast, the Weibull and Exponential distributions did not fit well. Upon closer inspection of the upper tail region, as presented in Figure 12, and the R^2 value, considering the tail region shown in Table 6, it is observed that the Lognormal distribution was a better fit than the Normal distribution at the upper tail region. The upper tail region is crucial for the calculation of failure rates. Therefore, the Lognormal distribution was chosen as the statistical model to be fitted to the measured values.

Table 6. R^2 values.

Statistical Model	Exponential	Lognormal	Normal	Weibull
R^2 Value	0.960	0.999	0.998	0.987
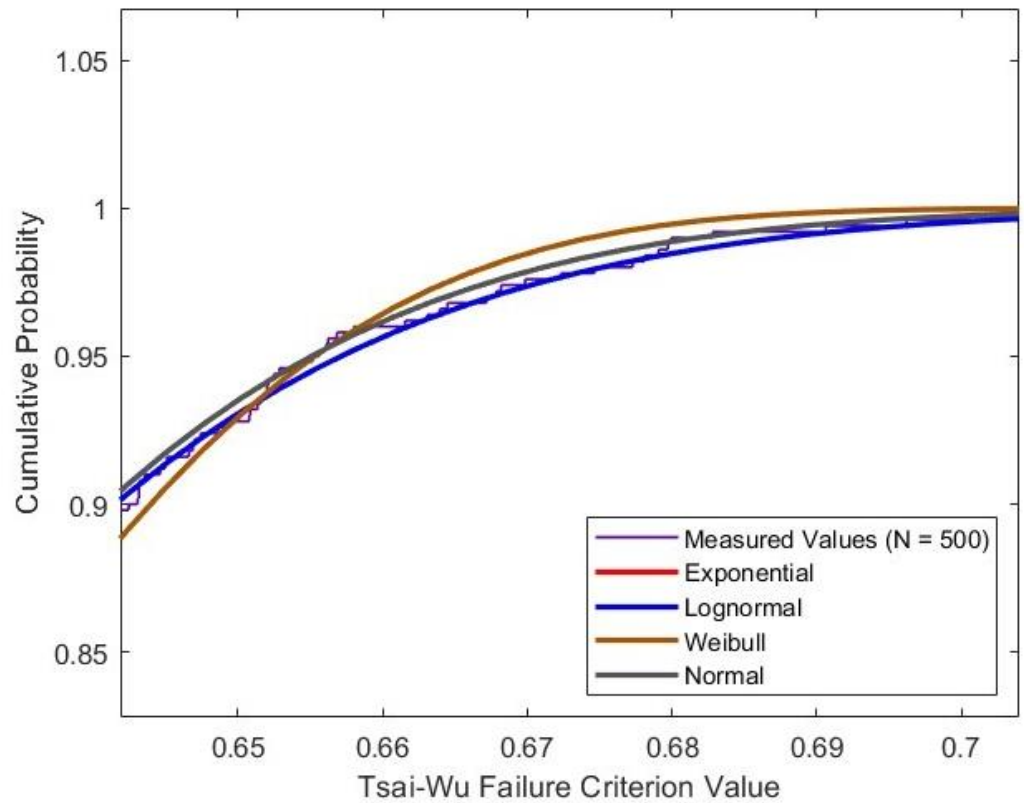
Figure 12. Statistical models fitted to measured values, zoomed in at the upper tail region.

3.5. Calculating the Response Surface

3.5.1. Parametric Correlation to Identify Most Influential Input Parameters

The parametric correlation matrix was calculated using the Spearman correlation method as described in Section 2.2 to identify the most influential input parameters. A sample size of 100 was used in the calculation. The sample size was large enough, based on previous studies by the authors on parametric correlation matrices associated with CFEC flow-lines [22]. The parametric correlation matrix is presented in Figure 13. The twenty most influential input parameters identified from the parametric correlation matrix are shown in Table 7. These twenty parameters were the ones with the most significant coefficients of correlation. These input parameters were used in the generation of the response surface.

Table 7. Most influential input parameters.

Parameter Group	Parameters	Level of Correlation
Loads	P, T	Moderate
Geometry	t	Moderate
Material properties	$E_2, \nu_{12}, \nu_{23}, \nu_{13}, G_{23}, G_{13}, \sigma_{ut1}, \sigma_{ut3}, \tau_{u23}, D, F_{12}, F_{13}, A, B$	Slight
	$E_1, \sigma_{ut2}, \tau_{u12}$	Low
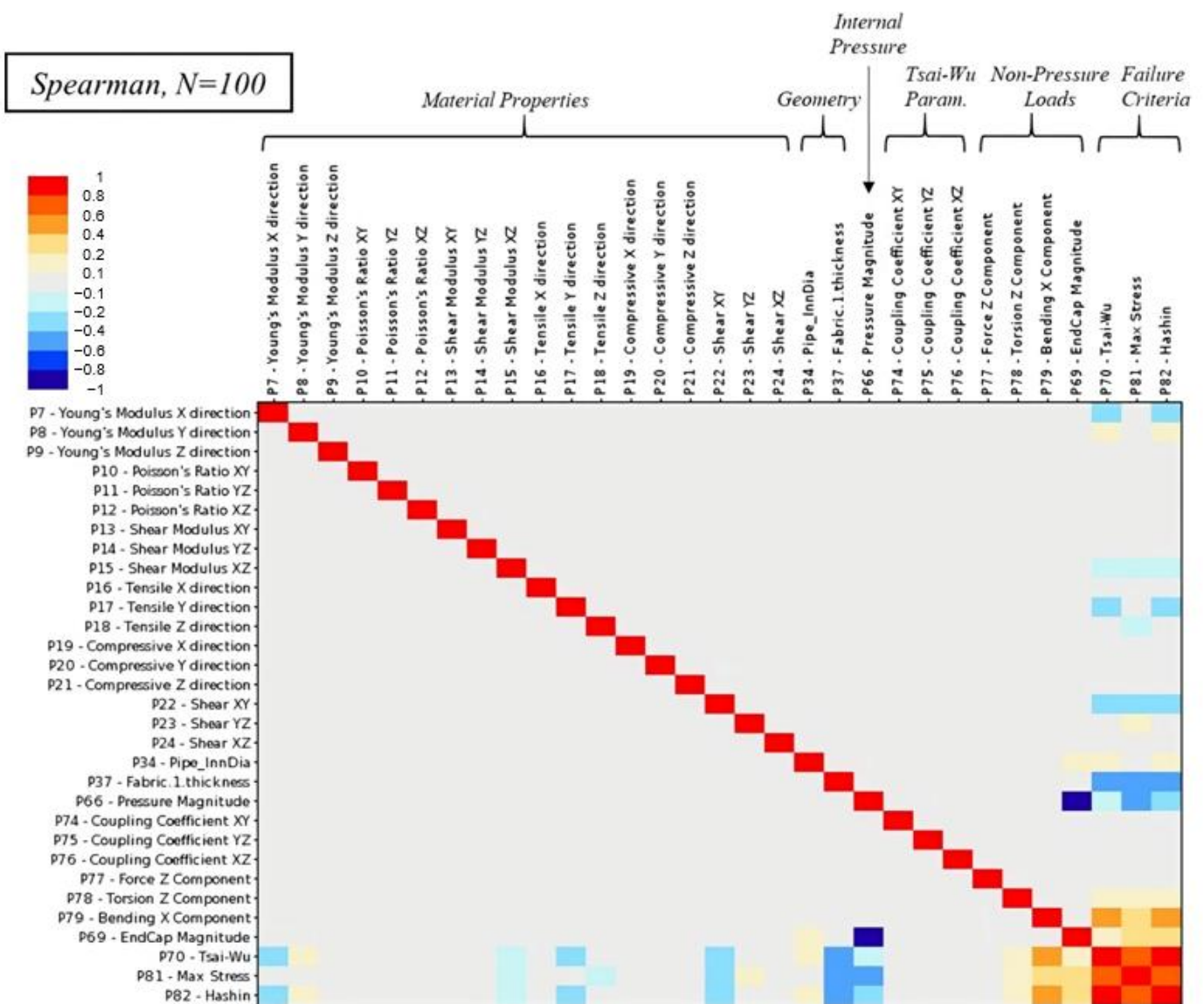
Figure 13. Parametric correlation matrix.

3.5.2. Range of Input Parameters

The range of input parameters used in the generation of the response surface is presented in Table 8. As previously discussed, the input parameters used in the response surface were the top twenty most influential input parameters found from the parametric correlation study presented in Section 3.5.1.

Table 8. Range of input parameters used in response surface.

Parameters	Symbol	Unit	Lower Limit	Upper Limit
Elastic Modulus	E_1	MPa	108,900	133,100
	E_2	MPa	7740	9460
Poisson's Ratio	ν_{12}, ν_{13}		0.243	0.297
	ν_{23}		0.36	0.44
Shear Modulus	G_{13}	MPa	4230	5170
	G_{23}	MPa	2790	3410
Tensile Strength	σ_{ut1}	MPa	2007.9	2454.1
	$\sigma_{ut2}, \sigma_{ut3}$	MPa	26.1	31.9
Shear Strength	τ_{u12}	MPa	54	66
	τ_{u23}	MPa	28.8	35.2
Internal pressure	P	MPa	6.21	7.59
Axial Force	A	N	18,000	22,000
Bending	B	Nm	1800	2200
Torsion	T	Nm	1800	2200
Tsai-Wu Constants	F_{12}, F_{13}		−1	1
Diameter	D	mm	100	150
Thickness	t	mm	0.18	0.22

4. Using Response Surfaces for Prediction of Failure Rates

In this section, the use of response surfaces for the prediction of failure rates is discussed. The failure rate is the probability of a component having a failure value exceeding 1.0. The failure rate is typically decided in combination with a risk assessment. In general, a 10^6 failure probability is low, while a 10^4 failure probability is high. A higher failure probability can be accepted if the failure consequence is low. The benefit of using response surfaces is that new sampling points are calculated almost instantly after they are generated. This provides time savings in the engineering evaluation of the design and, the case in this paper, the calculation of failure rates. The investigation was carried out as follows in this section. First, the statistical moments were compared between the samples generated from the measured values, the response surfaces, and their corresponding fitted Lognormal distributions. Second, the probability and cumulative distribution plots were compared. Last, the failure rates calculated from the response surface were compared against the base case. The workflow process used is presented in Figure 14.
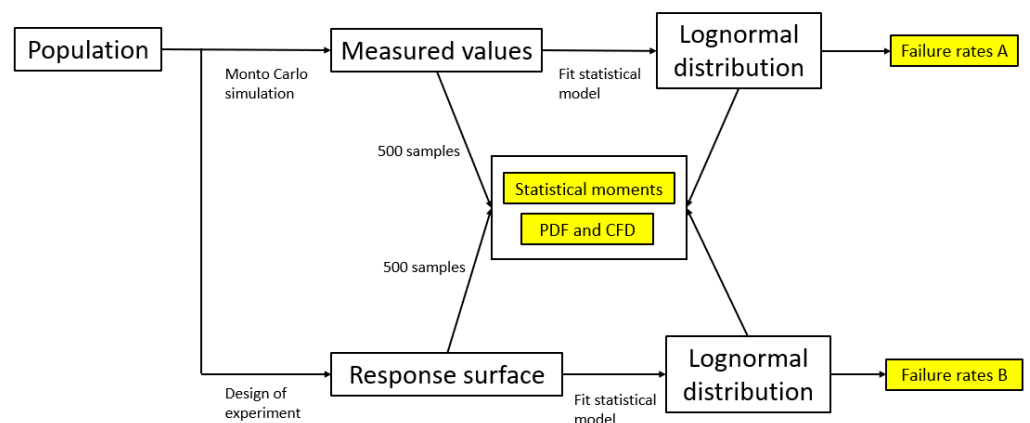
Figure 14. Workflow process.

4.1. Comparison of Statistical Moments

The comparison of the statistical moments is presented in Table 9. An explanation of "Source" in Table 9 is given in the following:

- Measured values, 500 samples. These were 500 sample points calculated directly from the finite element model. These 500 samples were considered the base case population.

- Lognormal distribution fitted to measured values: a Lognormal distribution fitted to 'Measured values, 500 samples'.
- Response surface, 500 samples. These were 500 sample points calculated directly from the response surface.
- Lognormal distribution fitted to response surface values: a Lognormal distribution fitted to 'Response surface, 500 samples'.
- The % differences were calculated with respect to 'Measured values, 500 samples' using Equation (16)

$$\% \text{ Difference} = \frac{Current\ value - Value\ @'Measured\ values,\ 500\ samples'}{Value\ @'Measured\ values,\ 500\ samples'} \times 100\% \quad (16)$$

Table 9. Comparison of statistical moments.

Source	Mean	Standard Deviation	Skewness	Kurtosis
Measured values, 500 samples	0.591	0.039	0.232	3.027
Lognormal distribution fitted to measured values	0.591 (0.0%)	0.039 (0.1%)	0.199 (−14.1%)	3.071 (1.4%)
Response surface, 500 samples	0.592 (0.3%)	0.036 (−8.5%)	0.209 (−9.8%)	2.980 (−1.6%)
Lognormal distribution fitted to response surface values	0.592 (0.3%)	0.036 (−8.6%)	0.182 (−21.7%)	3.059 (1.0%)

The following observations are made from the results presented in Table 9

- There are negligible differences in the mean values.
- The values obtained from the response surface, when fitted to the Lognormal distribution, have smaller standard deviation values, which are about 9% smaller than the measured values.
- There are large differences in the skewness values. The response surface skewness values are about 10% smaller than the measured values. Fitting the response surface values to a Lognormal distribution makes the skewness values even smaller, i.e., about 22% smaller than the measured values. In addition, fitting the measured values to a Lognormal distribution gives smaller skewness values of about 14% smaller than the measured values.
- There are only slight differences of below 2% in the kurtosis values.

4.2. Comparison of Probability and Cumulative Distribution Plots

The comparisons of the probability density and cumulative distribution plots are presented in Figures 15 and 16, respectively.

The following observations are made:

- The fitted distribution curves overlap the raw data, i.e., the measured and response surface sampled values.
- The response surface has a higher probability density at the most probable value; see area A in Figure 15.
- There are some differences in the tail regions in the cumulative probability distribution functions; see Figure 16. However, these differences are insignificant and lead to only negligible differences in the failure values calculated based on the upper tail region, as presented in Section 4.3.
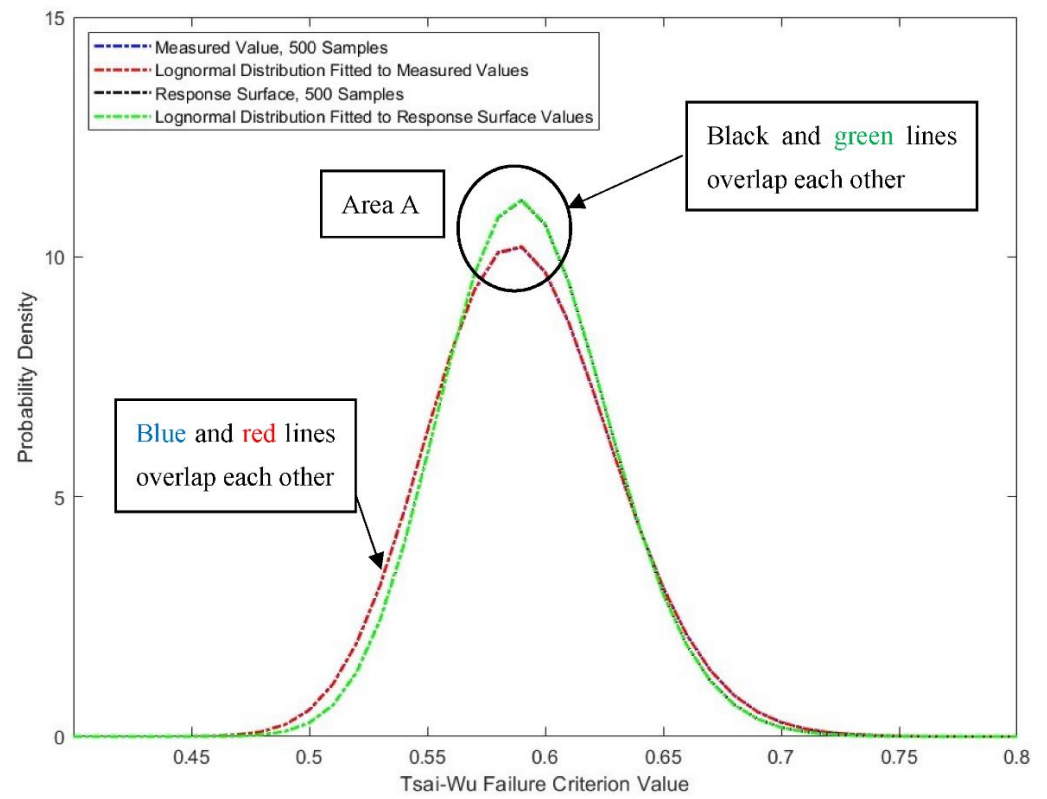
Figure 15. Comparison of probability density functions.
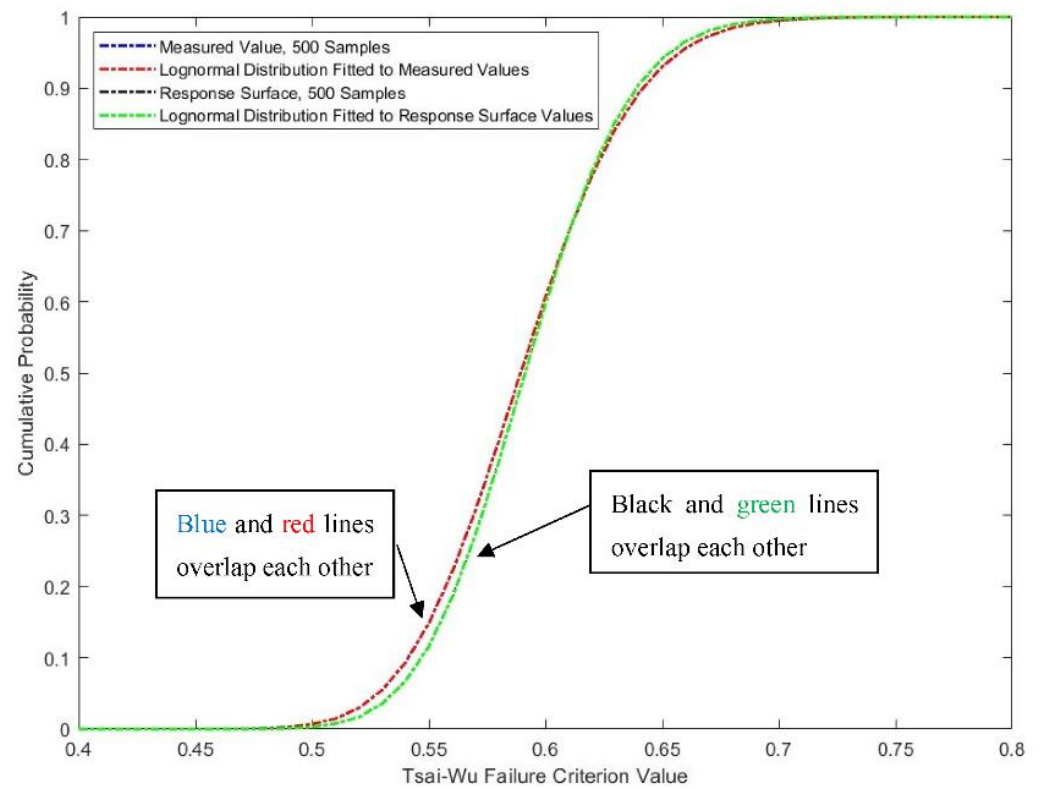
Figure 16. Comparison of cumulative probability distribution functions.

4.3. Comparison of Failure Values

The comparison of failure values at three different failure rates are presented in Table 10.

Table 10. Comparison of failure values.

Source	Failure Criterion	Failure Rate = 1 in 10^4	Failure Rate = 1 in 10^5	Failure Rate = 1 in 10^6
Lognormal distribution fitted to measured values	Maximum Stress	0.64	0.67	0.69
	Tsai-Wu	0.75	0.78	0.81
	Hashin	0.76	0.79	0.81
Lognormal distribution fitted to response surface values	Maximum Stress	0.64	0.66	0.68
	Tsai-Wu	0.74	0.77	0.79
	Hashin	0.75	0.78	0.80

Some notes on the large difference in the skewness values in Table 9 are made here. In general, it was harder for the skewness and kurtosis to be fitted well using an assumed probability distribution function, which in this case was the lognormal function. This is because both skewness and kurtosis are parameters that measure the shape of the probability density function. The assumed probability distribution (lognormal in this case) already has an assumed shape; therefore, it did not fit so well to the measured values at the peak region (see Figure 15). However, the failure values at different failure probability values, which are the parameters one would be concerned about within a design, are still reasonably close. This highlights that the more considerable differences in skewness did not significantly affect the results. Table 10 shows that the response surface model produced failure values that were very close to those resulting from the measured values. Therefore, it is a reliable tool for failure prediction of CEFC flow-lines under combined loading.

5. Optimising Response Surface Generation

5.1. Number of Input Parameters

This section investigates the number of input parameters used to generate the response surfaces. Twenty input parameters were used in the response surface presented in Section 4. Using a smaller number of input parameters requires a smaller design of experiment, as presented in Table 11. Choosing 10 input parameters instead of 20 input parameters results in a design of experiment that is less than one-third the size, leading to significant computational savings in the generation of the response surface. In this case, the 10 most influential input parameters out of the 20 were chosen. These were the parameters with the largest coefficients of correlation.

Table 11. Size of design of experiment for different numbers of input parameters.

Number of Input Parameters	5	10	15	20
Size of Design of Experiment, Number of Samples	27	149	287	551
Minimum Parametric Correlation Value	0.271	0.131	0.079	0.046

The effect on statistical moments, probability distributions, and predicted failure values are presented and discussed in Sections 5.1.1–5.1.3, The results show that using ten input parameters does not lead to any noticeable accuracy reduction in the calculated results. This is obvious in the case where five input parameters are used. The somewhat correlated parameters (having correlation coefficients between 0.131 to 0.271) to the failure value were excluded from generating the response surfaces.

5.1.1. Number of Parameters—Effect on Statistical Moments

The statistical moments are presented in Figure 17 for the response surfaces generated with different numbers of input parameters, together with the measured values (fitted and

raw values). The corresponding percentage differences versus the measured values are presented in Figure 18. The following observations are made:

- The mean values were not significantly affected when more than 10 input parameters are used where the differences were within 1%.
- The standard deviations were affected by the number of input parameters used. However, using the response surface would already result in a difference in the standard deviation of about 9%, as presented in Section 4.1. Using a smaller number of input parameters would increase this difference to about 20%.
- The skewness values were significantly affected by the number of input parameters used. However, using the response surface would already result in a difference in the standard deviation of about 14%, as presented in Section 4.1. Using a smaller number of input parameters would increase this difference to about 250%.
- The kurtosis values were not significantly affected when enough input parameters were used. However, the difference became as large as 60% when too few input parameters were used.
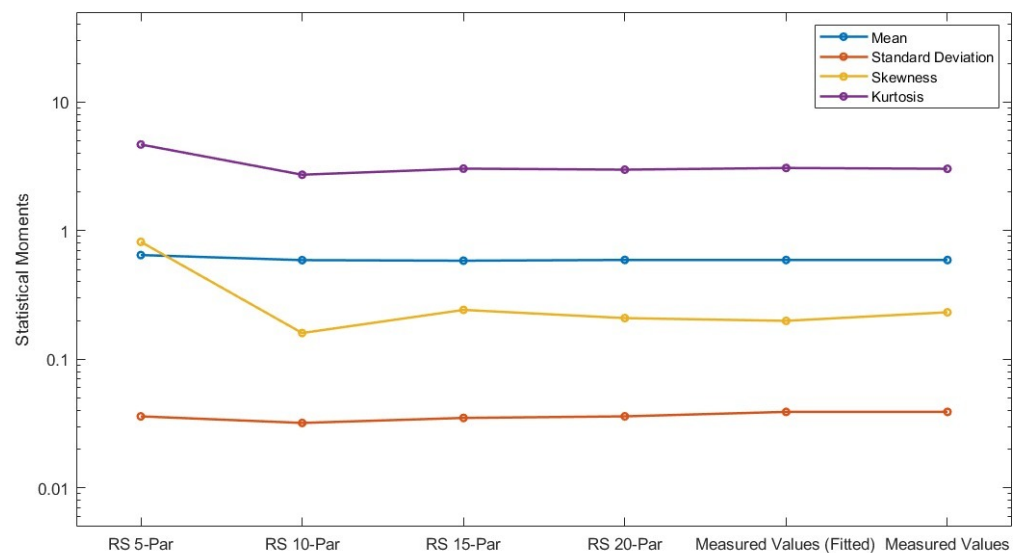
Figure 17. Number of parameters—effect on statistical moments.
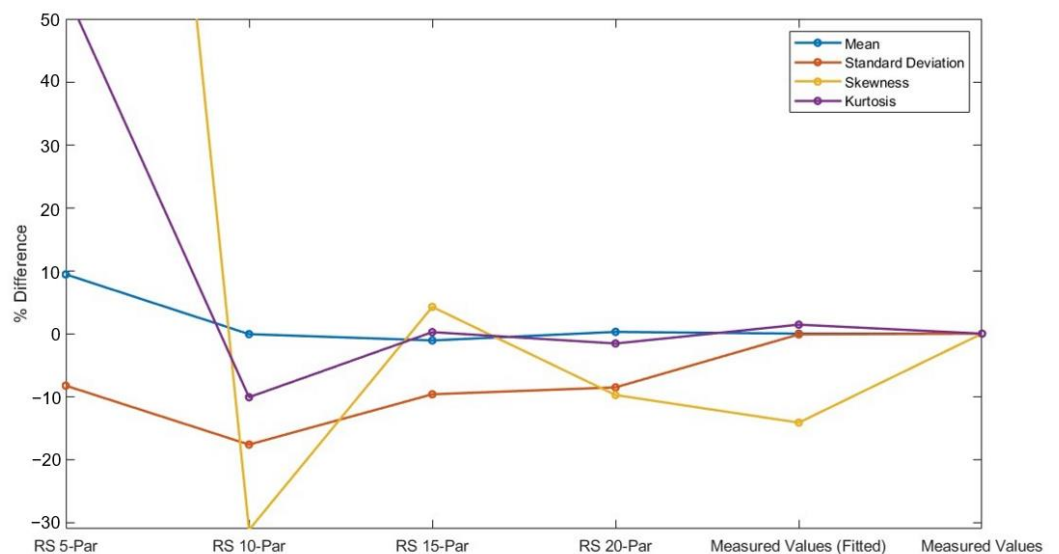
Figure 18. Number of parameters—effect on statistical moments (% difference).

5.1.2. Number of Parameters—Effect on Fitted Probability Distributions

The probability distributions (probability density and cumulative probability) fitted to response surface values with different numbers of input parameters were plotted together with the measured values and are presented in Figures 19–21.
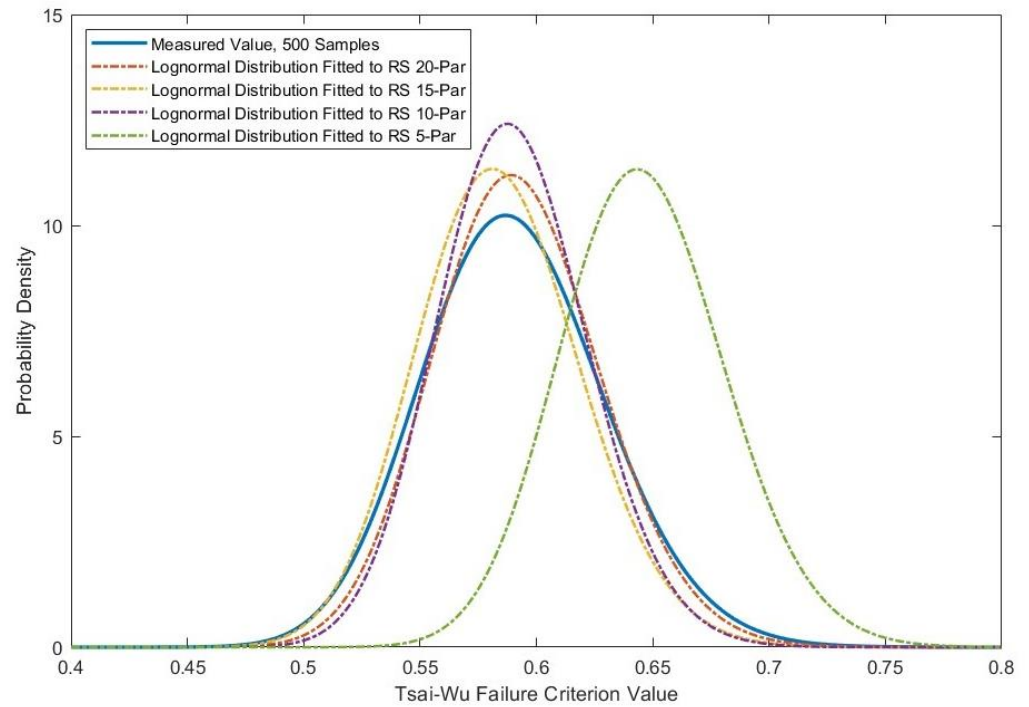
Figure 19. Number of parameters—effect on probability density functions.
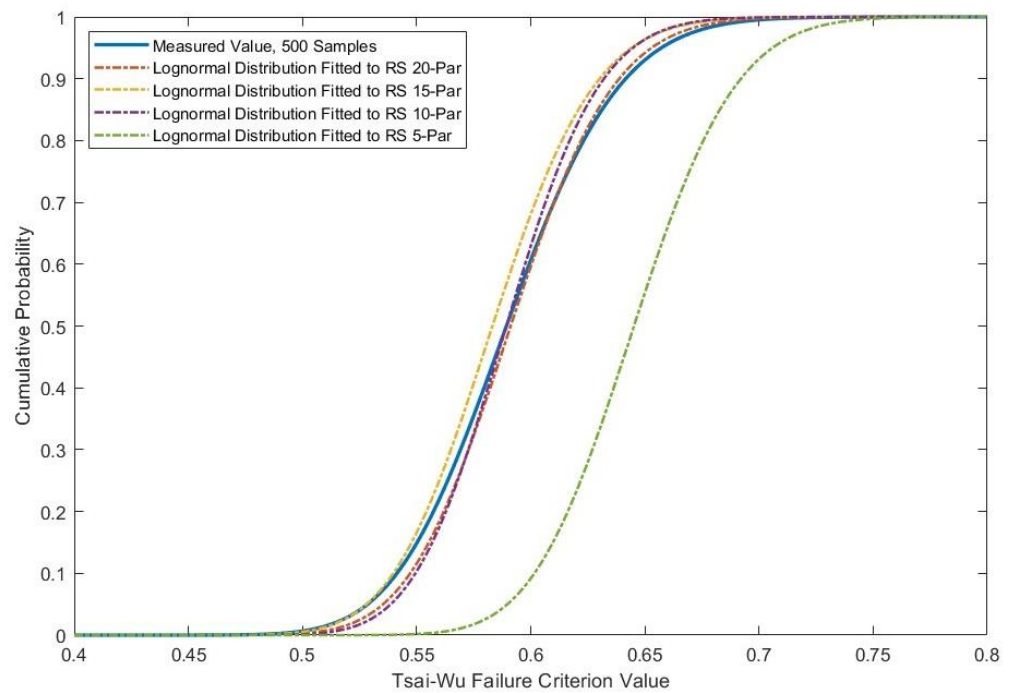
Figure 20. Number of parameters—effect on cumulative probability functions.
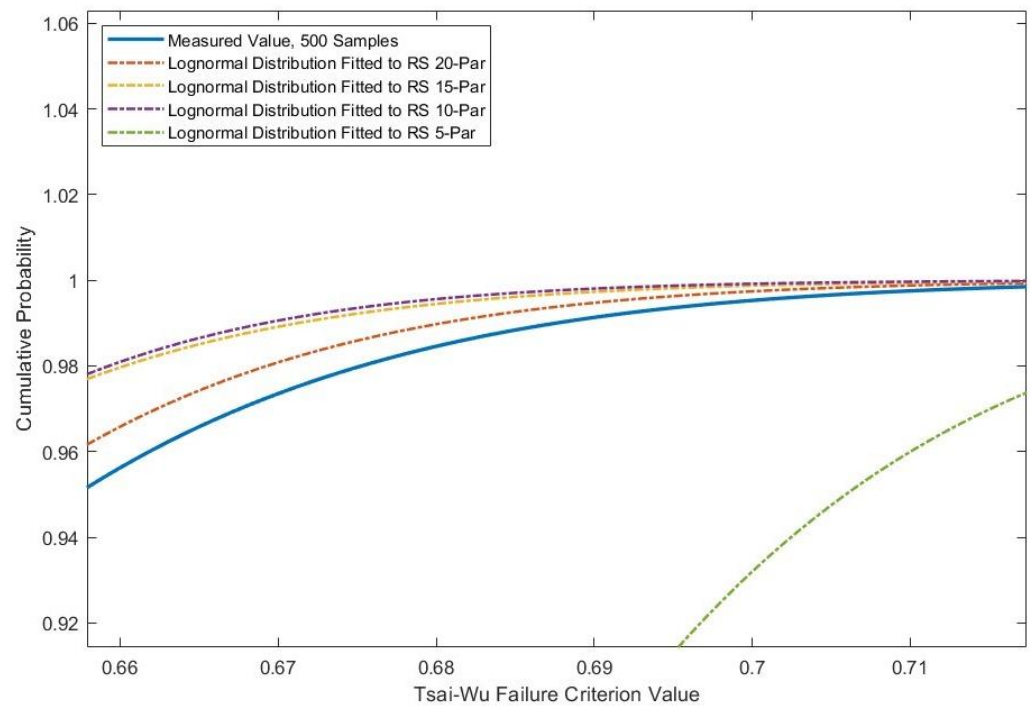
Figure 21. Number of parameters—effect on cumulative probability functions (zoomed in at upper tail region).

The following observations are made:

- In general, the probability distribution functions are highly inaccurate when a small number of input parameters, i.e., 5, is used.
- As presented in Figure 19, the probability density functions fitted from the response surfaces do not generally fit well with the measured values. A similar observation was also previously reported in Figure 15 and in Section 4.2.
- As presented in Figures 20 and 21, there are some differences in the cumulative probability distribution functions. These differences increase with decreasing number of input parameters. However, these do not significantly affect the upper tail regions and do not lead to large differences in the failure values calculated as presented in Section 5.1.3. Similar observations were also previously reported in Section 4.2.

5.1.3. Number of Parameters—Effect on Predicted Failure Values

Table 12 compares the predicted failure rates calculated from the Lognormal distributions fitted to response surfaces when a different number of input parameters was used. It is observed from the results that reducing the number of input parameters to ten, in general, do not lead to poor accuracy in the failure values predicted. The accuracy of the predicted failure values suffered when the number of input parameters was small. This can be expected because the failure values are calculated from distributions fitted to sampled values. As previously discussed in Section 5.1.2, the number of input parameters do not affect the fitted probability distributions, unless the number of input parameters is small, i.e., 5.

Table 12. Number of parameters—effect on predicted failure values.

Source	Failure Criterion	Failure Rate = 1 in 10^4	Failure Rate = 1 in 10^5	Failure Rate = 1 in 10^6	% Diff, Failure Rate = 1 in 10^4	% Diff, Failure Rate = 1 in 10^5	% Diff, Failure Rate = 1 in 10^6
Lognormal distribution fitted to measured values	Maximum Stress	0.64	0.67	0.69	-	-	-
	Tsai-Wu	0.75	0.78	0.81	-	-	-
	Hashin	0.76	0.79	0.81	-	-	-
Lognormal distribution fitted to response surface values (20 input parameters)	Maximum Stress	0.64	0.66	0.68	0.0	−1.5	−1.4
	Tsai-Wu	0.74	0.77	0.79	−1.3	−1.3	−2.5
	Hashin	0.75	0.78	0.80	−1.3	−1.3	−1.2
Lognormal distribution fitted to response surface values (15 input parameters)	Maximum Stress	0.64	0.67	0.69	−1.6	−3.0	−1.4
	Tsai-Wu	0.75	0.78	0.81	−2.7	−2.6	−3.7
	Hashin	0.76	0.79	0.81	−2.6	−2.5	−2.5
Lognormal distribution fitted to response surface values (10 input parameters)	Maximum Stress	0.64	0.66	0.68	0.0	−1.5	−1.4
	Tsai-Wu	0.74	0.77	0.79	−4.0	**−5.1**	**−6.2**
	Hashin	0.75	0.78	0.8	−1.3	−1.3	−1.2
Lognormal distribution fitted to response surface values (5 input parameters)	Maximum Stress	0.63	0.65	0.68	**15.6**	**14.9**	**15.9**
	Tsai-Wu	0.73	0.76	0.78	**5.3**	**5.1**	3.7
	Hashin	0.74	0.77	0.79	2.6	2.5	2.5

5.2. Size of Response Surface

In this section, the effects of response surfaces sizes are studied. Two larger response surfaces were compared against the original surface size used in Sections 3, 4 and 5.1. These larger response surfaces were named 'larger size' and 'extremely large size'. The number of input parameters used to generate the response surfaces was the same, i.e., 20, while the range of diameter and ply thickness is varied. The diameters and ply thicknesseses considered are presented in Table 13.

Table 13. Range of diameters and ply thicknesses studied.

	Diameter (mm)	Thickness (mm)
Base Case	100–150	0.18–0.22
Larger Size	75–175	0.14–0.26
Extremely Larger Size	50–200	0.10–0.30

The effect on statistical moments, probability distributions, and predicted failure values are presented and discussed in Sections 5.2.1–5.2.3 The results show that the huge response surface leads to inaccurate skewness values and probability distribution functions. However, the size of the response surface does not significantly affect the upper tail regions of the probability distributions and consequently leads to only minor differences in predicted failure rates if it is not too large, as demonstrated in the 'larger size' response surface.

5.2.1. Size of Response Surface—Effect on Statistical Moments

The statistical moments are presented in Figure 22 for the response surfaces generated with different diameter ranges and ply thickness and the measured values (fitted and raw values). The corresponding percentage differences versus the measured values are presented in Figure 23. The following observations are made:

1. In general, the differences in statistical moments calculated increased with the size of the response surface used.
2. The differences in the mean values increase with the size of the response surface used but were within 10% for 'extremely large size'.
3. The response surface size has limited or no influence on the standard deviation values. The differences in the standard deviation are within approximately 10%, which were like that of the 'base case', which had 8.5%.

4. The skewness is strongly affected by the response surface size. For the 'larger size' and 'extremely large size', the differences were as much as 40%.
5. The differences in the kurtosis values increased with the size of the response surface used but were within 10% for 'extremely large size'.
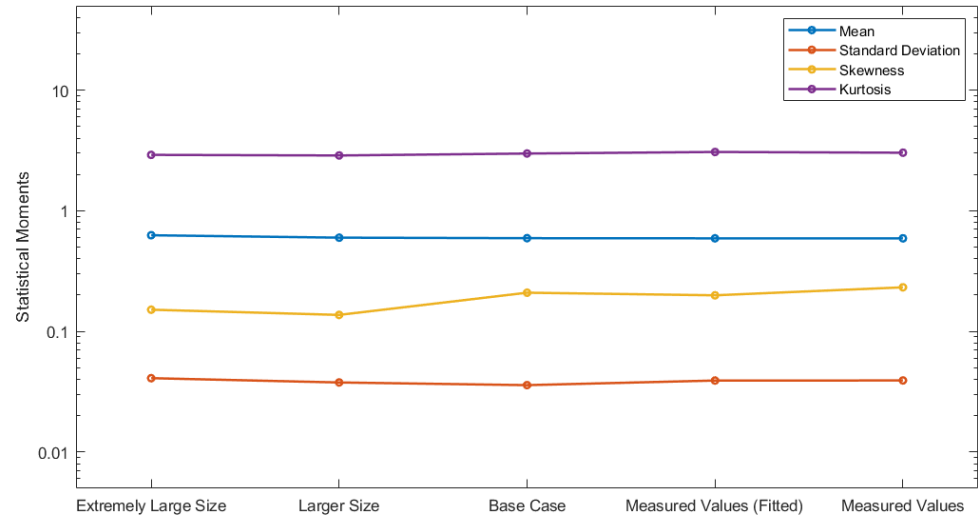
Figure 22. Size of response surface—effect on statistical moments.
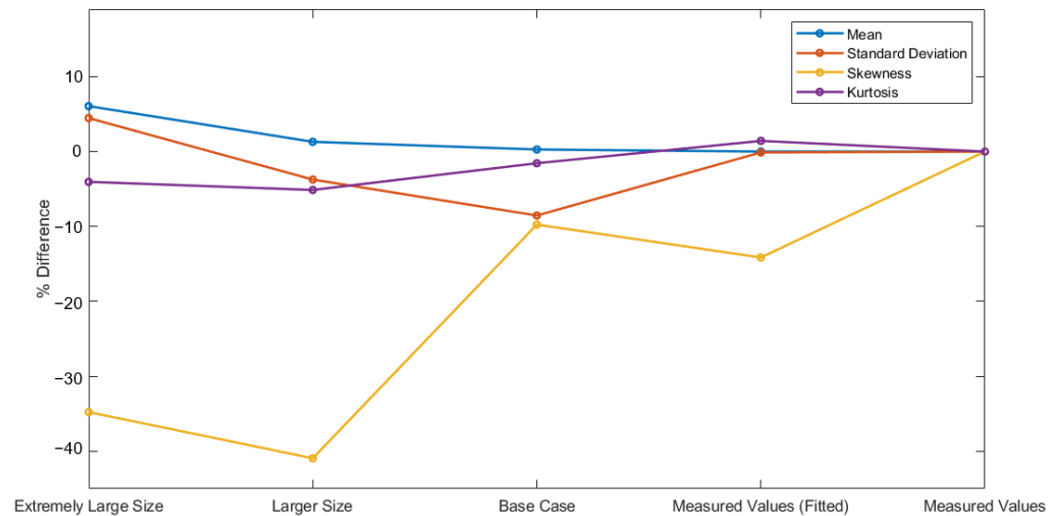
Figure 23. Size of response surface—effect on statistical moments (% difference).

5.2.2. Size of Response Surface—Effect on Fitted Probability Distributions

The probability distributions (probability density and cumulative probability) fitted to response surface values with different response surface sizes are plotted together with the measured values (fitted and raw values) and presented in Figures 24–26.

The following observations are made:

- In general, using 'extremely large size' results in significant differences in the probability distributions.
- As presented in Figure 24, the probability density functions fitted from the response surfaces do not generally fit well with the measured values. The 'extremely large size' probability distribution function is especially far away from that of the measured values.
- As shown in Figure 25, the cumulative probability distributions of 'base case' and 'larger size' were close to those of the measured values. Furthermore, as presented in

Figure 26, these differences became more minor at the upper tail regions. As observed in the probability density functions, the 'extremely large size' cumulative probability function is especially far away from that of the measured values.
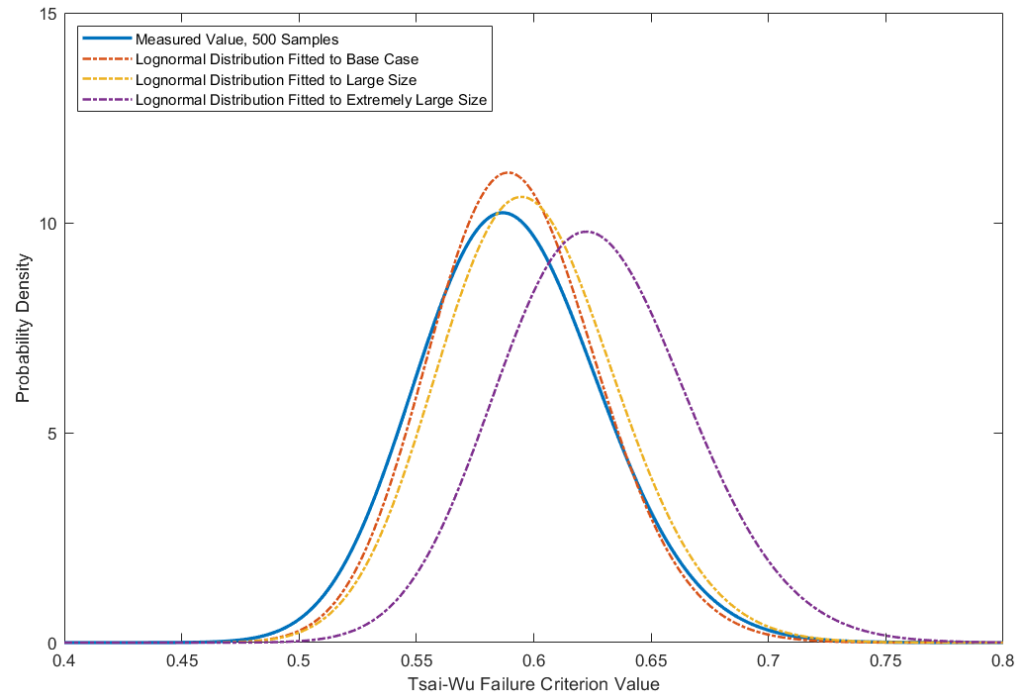
Figure 24. Size of response surface—effect on probability density functions.
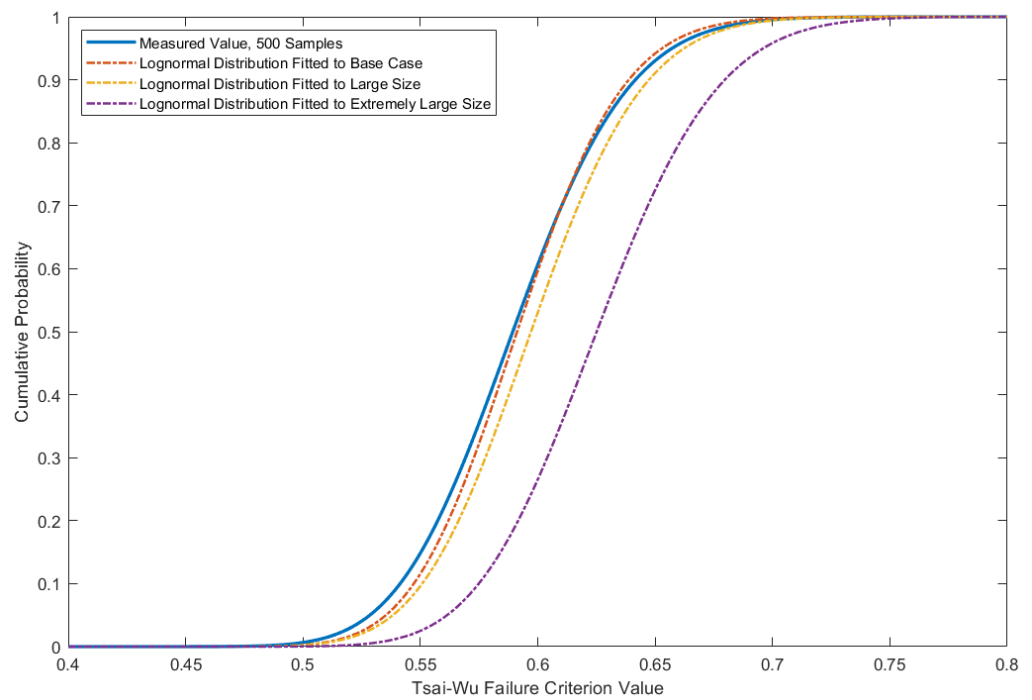
Figure 25. Size of response surface—effect on cumulative probability functions.
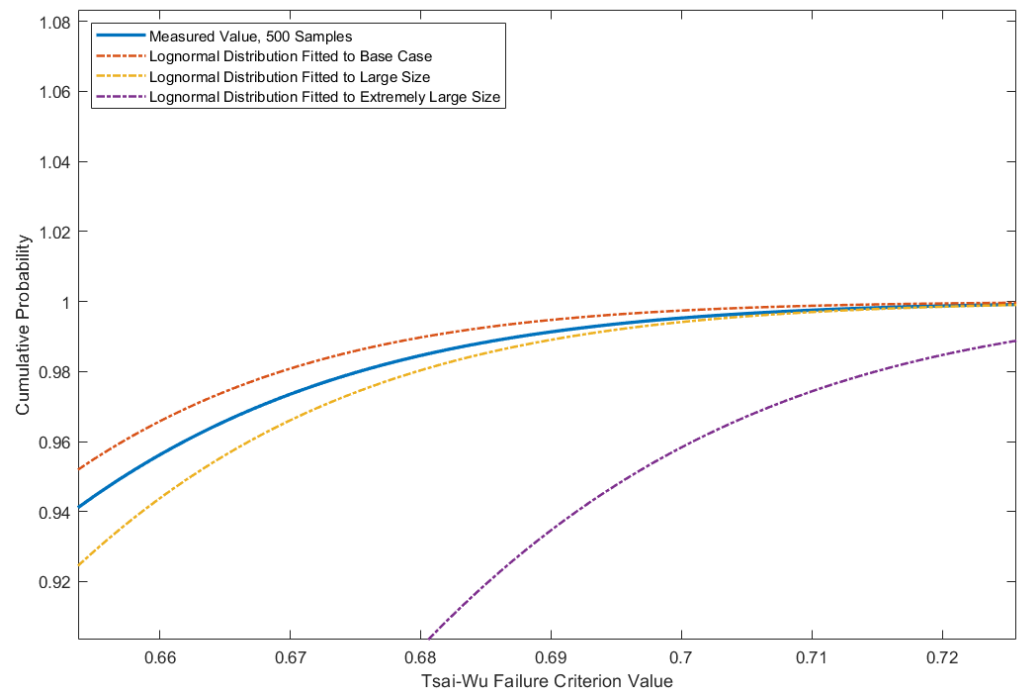
Figure 26. Size of response surface—effect on cumulative probability functions (zoomed in at upper tail region).

5.2.3. Size of Response Surface—Effect on Predicted Failure Values

Table 14 compares the predicted failure rates calculated from the Lognormal distributions fitted to response surfaces with different ranges of diameter and ply thickness. It is observed that the size of the response surfaces did not significantly affect the predicted failure values. A larger response surface, in general, would lead to more considerable differences in the predicted failure values. Most of the differences were below 5% except for the Tsai-Wu failure value for the 'extremely large size' response surface.

Table 14. Number of parameters—effect on predicted failure values.

Source	Failure Criterion	Failure Rate = 1 in 10^4	Failure Rate = 1 in 10^5	Failure Rate = 1 in 10^6	% Diff, Failure Rate = 1 in 10^4	% Diff, Failure Rate = 1 in 10^5	% Diff, Failure Rate = 1 in 10^6
Lognormal distribution fitted to measured values	Maximum Stress	0.64	0.67	0.69	-	-	-
	Tsai-Wu	0.75	0.78	0.81	-	-	-
	Hashin	0.76	0.79	0.81	-	-	-
Lognormal distribution fitted to base case response surface values	Maximum Stress	0.64	0.66	0.68	0.0	−1.5	−1.4
	Tsai-Wu	0.74	0.77	0.79	−1.3	−1.3	−2.5
	Hashin	0.75	0.78	0.80	−1.3	−1.3	−1.2
Lognormal distribution fitted to larger size response surface values	Maximum Stress	0.63	0.65	0.67	−1.8	−1.9	−2.1
	Tsai-Wu	0.75	0.78	0.81	−0.1	−0.1	−0.3
	Hashin	0.75	0.77	0.80	−1.2	−1.4	−1.5
Lognormal distribution fitted to extremely large response surface values	Maximum Stress	0.63	0.66	0.67	−1.4	−1.8	−2.1
	Tsai-Wu	0.80	0.83	0.85	5.7	5.6	5.6
	Hashin	0.76	0.79	0.81	0.6	0.4	0.2

5.3. Recommendations for Optimisation of Response Surface

Based on the findings obtained in Sections 5.1 and 5.2, the following recommendations are made for the optimisation of the response surface:

- Reduce the input parameters selected to generate the response surface by only selecting the parameters with parametric correlation coefficients greater than $+/-0.15$.

- Consider using a larger response surface to maximise flexibility if the accuracy in the predicted failure values is not extremely important. A larger response surface would lead to some decreased accuracy in the results.

6. Conclusions

In this paper, the use of the Kriging response surface method for the estimation of failure values in carbon-fibre-epoxy composite flow-lines under the influence of stochastic processes was investigated. The following conclusions are made:

- In general, the response surface method produced predicted failure results close to those of the measured values. Most errors were minor unless too few input parameters are selected to generate the response surface and/or the size of the response surface was too large.
- The response surfaces do not accurately represent the skewness values in general; there was at least a 9% difference in the results. However, this is not of practical significance as it did not affect the prediction of failure values.
- In general, using more input parameters increases the accuracy of the response surface. However, it also increases the time required to generate the response surface, as the design of experiment will increase in size.
- It is recommended to select input parameters with correlation coefficients greater than $+/-0.15$, i.e., input parameters that are slightly correlated. In this present study, this results in about 10 input parameters.
- In general, a more extensive response surface leads to reduced accuracy. However, this enables greater flexibility in its utilisation as a more comprehensive range of input parameters is covered.
- The response surface enables more rapid design optimisation process than using a brute force method; the computation of the failure values is instantaneous.

Author Contributions: Conceptualization, Y.X.; methodology, Y.X.; software, Y.X., W.X. and V.B.; validation, Y.X and W.X.; formal analysis, Y.X., W.X. and V.B.; investigation, Y.X., W.X and V.B.; resources, Y.X.; data curation, W.X.; writing—original draft preparation, Y.X.; writing—review and editing, Y.X.; visualization, Y.X. and W.X; supervision, Y.X. and V.B.; project administration, Y.X.; funding acquisition, Y.X. All authors have read and agreed to the published version of the manuscript.

Nomenclature

σ_h	Hoop stress
σ_l	Longitudinal stress
σ_1	Principle stress in x-direction
σ_2	Principle stress in y-direction
σ_3	Principle stress in z-direction
τ_{12}	Shear stress in xy-plane
τ_{23}	Shear stress in yz-plane
τ_{13}	Shear stress in xz-plane
σ_{uc1}	Compressive strength limit in x-direction
σ_{uc2}	Compressive strength limit in y-direction
σ_{uc3}	Compressive strength limit in z-direction
σ_{ut1}	Tensile strength limit in x-direction
σ_{ut2}	Tensile strength limit in y-direction
σ_{ut3}	Tensile strength limit in z-direction

τ_{u12}	Shear strength limit in xy-plane
τ_{u23}	Shear strength limit in yz-plane
τ_{u13}	Shear strength limit in xz-plane
$\rho_{rgX,rgY}$	Spearman correlation coefficient
$cov\left(r_{gX}, r_{gY}\right)$	Covariance of the rank variable
SD_{rg_X}	Standard deviation of the rank variable g_X
SD_{rg_Y}	Standard deviation of the rank variable g_Y
D	Flow-line Diameter
t	Flowline wall thickness

References

1. U.S. Energy Information Administration. U.S. Average Depth of Crude Oil and Natural Gas Wells. 2020. Available online: https://www.eia.gov/dnav/ng/hist/e_ertw0_xwd0_nus_fwa.htm (accessed on 12 April 2020).
2. Global Data. *H1 2019 Global Length and Capital Expenditure Outlook for Oil and Gas Pipelines—Natural Gas Pipelines Take Lead in New-Build Projects*; Global Data: London, UK, 2019; p. 48.
3. ICF International for The INGAA Foundation. North America Midstream Infrastructure through 2035: Capitalising on Our Energy Abundance. INGAA Foundation. 2020. Available online: https://www.igaa.org/File.aspx?id=21527&v=6be6e34a (accessed on 12 April 2020).
4. Yang, C. Design and analysis of composite pipe joints under tensile loading. *J. Compos. Mater.* **2000**, *34*, 332–349. [CrossRef]
5. Jha, V.; Dodds, N.; Finch, D.; Latto, J.; Karabelas, G.; Anderson, T.A.; Baehmann, P.; Vermilyea, M.E. Flexible Fiber-reinforced Pipe for 10,000-foot Water Depths: Performance Assessments and Future Challenges, OTC-25393-MS. In Proceedings of the Offshore Technology Conference, Houston, TX, USA, 5–8 May 2014.
6. Bazán, F.; Beck, A. Stochastic process corrosion growth models for pipeline reliability. *Corros. Sci.* **2013**, *74*, 50. [CrossRef]
7. Oliveira, N.; Bisaggio, H.; Netto, T. Probabilistic Analysis of the Collapse Pressure of Corroded Pipelines. In Proceedings of the International Conference on Offshore Mechanics and Artic Engineering, OMAE2016-54299, Busan, Korea, 19–24 June 2016.
8. Jia, B.; Yu, X.; Yan, Q. A new sampling strategy for Kriging-based response surface method and its application in structural reliability. *Adv. Struct. Eng.* **2016**, *20*, 564–581. [CrossRef]
9. Simpson, T.; Mauery, T.; Korte, J.; Mistree, F. *Comparison of Response Surface and Kriging Models for Multidisciplinary Design Optimisation*; American Institute of Aeronautics and Astronautics: St. Louis, MO, USA, 2012. [CrossRef]
10. Gupta, S.; Manohar, C. An improved response surface method for the determination of failure probability and importance measures. *Struct. Saf.* **2004**, *26*, 123–139. [CrossRef]
11. Tsai, S.W.; Wu, E.M. A general theory of strength for anisotropic materials. *J. Compos. Mater.* **1971**, *5*, 58–80. [CrossRef]
12. Hashin, Z. Failure criteria for unidirectional fiber composites. *J. Appl. Mech.* **1980**, *47*, 329. [CrossRef]
13. ANSYS®. Academic Research Mechanical, Release 17.0, Help System, Element Reference, Chapter I, SHELL181, ANSYS, Inc. 2017. Available online: https://www.mm.bme.hu/~{}gyebro/files/ans_help_v182/ans_elem/Hlp_E_SHELL181.html (accessed on 1 August 2020).
14. Feng, N.L.; Malingam, S.D.; Irulappasamy, S. Bolted Joint Behaviour of Hybrid Composites. In *Failure Analysis in Biocomposites, Fibre-Reinforced Composites and Hybrid Composites*; Jawaid, M., Thariq, M., Saba, N., Eds.; Woodhead Publishing: Sawston, UK, 2019; pp. 79–95.
15. Gol'denblat, I.I.; Kopnov, V.A. Strength of glass-reinforced plastics in the complex stress state. *Polym. Mech.* **1965**, *1*, 54–59. [CrossRef]
16. Clouston, P.; Lam, F.; Barrett, D. Interaction term of Tsai-Wu theory for laminated veneer. *J. Mater. Civ. Eng.* **1998**, *10*, 112–116. [CrossRef]
17. Li, S.; Sitnikova, E.; Liang, Y.; Kaddour, A.S. The Tsai-Wu failure criterion rationalised in the context of UD composites. *Compos. Part A Appl. Sci. Manuf.* **2017**, *102*, 207–217. [CrossRef]
18. Spearman, C. Correlation calculated from faculty data. *Br. J. Psychol.* **1910**, *3*, 271–295.
19. Box, G.E.P.; Wilson, K.B. On the experimental attainment of optimum conditions (with discussion). *J. R. Stat. Soc. Ser. B* **1951**, *13*, 1–45.
20. Krige, D.G. A Statistical Approach to Some Mine Valuations and Allied Problems at the Witwatersrand. Master's Thesis, University of Witwatersrand, Johannesburg, South Africa, 1951.
21. Arcieri, E.V.; Baragetti, S.; Bozic, Z. Application of design of experiments to foreign object damage on 7075-T6. *Procedia Struct. Integr.* **2021**, *31*, 22–27. [CrossRef]
22. Xing, Y.H.; Wu., X.; Buratti, V. The correlation and determination matrices associated with the burst design of a subsea carbon-fibre-epoxy composite flow-line. *IOP Conf. Ser. Mater. Sci. Eng.* **2019**, *700*, 012021. [CrossRef]